Nozzle Flow Control Through D-Shape Rib With Abrupt Change in Area at Mach One: A Comprehensive CFD Approach

Newaz Md. Ashif[1], Sher Afghan Khan[1], Mohd Azan Mohammad Sapardi[1], S. M. Afzal Hoq[2]

[1] Department of Mechanical and Aerospace Engineering, Faculty of Engineering, IIUM, Gombak Campus, Kuala Lumpur-53100, Malaysia

[2]Department of Science, Faculty of Engineering, IIUM, Kuala Lumpur-53100, Malaysia

Abstract: The development of the enlarged duct appears to be of interest to many practical problems in the automobile industry and aerospace vehicles, such as unguided rockets, missiles, and the space shuttle. The study of space shuttles and high-performance military aircraft has made the investigation of turbulent flow in separated regions a vital topic of study. Researchers are also interested in turbulent flow in transonic and supersonic flow. There is considerable relief for the flow when it separates and expands once the area of the larger duct suddenly increases. There are two areas where the shear layer emerges: the separated flow and the main flow. Considerable drag results from the split stream line becoming reattached to the duct, creating a recirculation zone where the pressure is lower than that of the surrounding air. Flow from a converging nozzle is suddenly exhausted to a larger diameter. The duct diameter is 20 mm. Base pressure management using a D-shaped rib as a passive control mechanism is the primary focus of this study. The passive control was located at various positions, with a length-to-diameter ratio (L/D) of 0.5, 1, 1.5, 2, and 3. Numerical simulations were conducted for 0.5, 1, and 1.5 mm rib radii. Results indicated that the D-shape rib with a 0.5 mm radius is ineffective, except at nozzle pressure ratios of 4 and 5. The maximum increase in the base pressure is attained for a rib radius of 1.5 mm, and a moderate rise is obtained for a 1 mm radius, as this 1 mm height of the rib appears to be ineffective. It is observed that the rib locations at L/D = 2 and 3 are inadequate, as the flow becomes attached to the wall around L/D = 1 to 1.5. Hence, one can select the rib radius and height based on the user's requirements, as the flat surface of the rib faces the shear layer after being exhausted from the nozzle.

Keywords: D-shape Rib, L/D Ratio, Nozzle Pressure Ratio, Mach Number, Expansion Level

1. Introduction:

Since the inception of fluid science, turbulence has remained enigmatic. It exists in both natural and pretend flows around us, and recognizing it is essential. One must comprehend the concept of turbulence to manage the drag associated with turbulent flows. In some cases, turbulence is needed, such as when fluids mix or when skin friction drag increases are required. However, turbidness is generally unwanted in engineering flows and should be addressed to reduce energy input. In both engineering applications and real-world processes, turbulent drag has significant ecological and economic implications. Various methods are employed to utilize fossil fuels.

Suddenly, expanded flow fields are employed in various fascinating and valuable situations, including parallel diffusers, propulsion systems, and combustion chambers. These flows have been studied due to the need to manage such flow fields. Because they produce the desired outcome without requiring additional mechanisms, as active control does, passive control mechanisms have long attracted the attention of scientists for their simplicity and ease of use. However, passive control remains a liability with the system, unlike launch vehicles, which are discarded once the propellant is completely burned. One of the most significant advantages of dynamic control is that it can be used as needed.

Numerous applications, such as high-speed aircraft, jet engines, rocket motors, rapid entry into a planetary atmosphere, gas pipelines, and commercial uses like abrasive blasting, utilize the effects of compressible flow. While incompressible flow primarily operates with constant density, compressible flow addresses a variable range of density flows, spanning from subsonic to supersonic.

The analysis of turbulent flow remains an area of ongoing research, driven by the development of high-speed missiles, unguided rockets, and supersonic military aircraft. Flow separation, recirculation, and reattachment are complex characteristics of an axisymmetric expansion flow field. The two primary regions where a shear layer may separate in this flow field are the recirculation region and the central flow region—the point where the separating streamline contacts the wall is referred to as the reattachment line. A wealth of information regarding sudden expansion issues is available in the literature, yet it pertains to specific flow and geometric parameter scenarios. Reducing turbulent drag can help mitigate global warming by lowering CO2 emissions from the combustion of fossil fuels. Therefore, efforts should focus on eliminating the near-wall organized structures that significantly contribute to drag production. These near-wall structures can be altered using passive or active control techniques. While passive methods such as splitter plates, riblets, Gurney flaps, bleed, and superhydrophobic surfaces are straightforward to implement, the resulting drag reduction is relatively modest. In contrast, active control methods can achieve substantial reductions in skin friction drag. Despite the challenges associated with implementing active control strategies and their need for feedback loops, the potential benefits of exploring innovative active control methods are enticing.

2. Literature Review:

The base pressure control in suddenly expanded flows has been extensively studied due to its direct impact on base drag reduction, constituting a significant portion of the total aerodynamic resistance in high-speed aerospace applications. Flow control strategies are broadly classified into active and passive techniques. Active control methods, such as microjets, have effectively enhanced base pressure by altering the flow field near the recirculation zone; however, they require external energy input, which complicates their implementation in real-world aerospace systems where energy efficiency is a priority [1]. While active control techniques enable on-demand flow regulation, their dependence on external energy renders them less practical for many aerospace applications. In contrast, passive control mechanisms such as splitter plates and ribs modify the aerodynamic flow without requiring additional energy, making them more viable for practical use. E. Rathakrishnan [2] demonstrated that splitter plates reduce base drag by changing the recirculation zone. Still, their effectiveness depends on placement and aspect ratio, which may not always be adaptable to various aerodynamic configurations.

E. Rathakrishnan [3,4] researched the use of ribs as passive control devices in suddenly expanded flows, demonstrating that these structures generate secondary vortices that interact with the primary flow, thereby enhancing base pressure and reducing drag. These studies form the foundational work on rib-based passive control, but they primarily consider simple rib geometries without examining the influence of corrugation. The present study builds upon these findings by introducing corrugated ribs, which further manipulate the flow structure and improve pressure recovery. Vijayaraja et al. [5] highlighted the significance of rib geometry in determining the effectiveness of passive flow control, while Sethuraman et al. [6,7] emphasized the role of rib height and placement in minimizing the recirculation zone. Although these studies provided valuable insights, they did not explore how different rib geometries affect flow oscillations and shock-boundary layer interactions. The present study extends this research by systematically analyzing how corrugated ribs influence base pressure fluctuations, offering a more comprehensive understanding of their aerodynamic impact.

Despite previous research on passive control methods, certain limitations remain unaddressed. Khan et al. [8–12] discussed various rib designs but did not quantify their

effects on vortex shedding, shock standoff distance, or transient pressure fluctuations. These gaps are addressed in the current study, which conducts a detailed computational and experimental analysis of the role of corrugated ribs in regulating base pressure. The CFD method has proven to be an essential tool in studying base pressure control mechanisms [10,11]. Ambareen et al. [12,13] utilized the k-epsilon turbulence model to analyze the consequence of ribs on base pressure, confirming that CFD simulations can accurately capture the flow dynamics in suddenly expanded flows. However, their study did not focus on corrugated ribs or validate the numerical results with experimental data.

The impact of rib geometry on base pressure has also been explored through the finite volume method (FVM), as demonstrated by Ambareen et al. [14]. While this study established the capability of FVM in simulating complex flow patterns, it did not investigate the aerodynamic trade-offs associated with different rib configurations. The present research provides an intense analysis by comparing multiple rib geometries and evaluating their effects on pressure recovery, turbulence intensity, and overall aerodynamic efficiency. Beyond rib-based passive control, studies on forward-facing cavities have shown their potential to reduce drag and mitigate aerodynamic heating [15]. Heubner and Utreja [16] investigated the influence of forward-facing cavities in hypersonic flow, demonstrating that they alter shock structures and reduce aerodynamic heating. While their findings contribute to the broader field of flow control, they did not consider passive rib configurations, which could offer similar benefits without compromising structural integrity.

Lorite et al. [17] explored optimized rear cavity designs for drag reduction, revealing that cavity geometry is crucial in minimizing aerodynamic resistance. Sanmiguel [18] investigated the drag reduction produced by combining multiple cavities in the recirculation zone of a bluff body. However, their study focused on blunt-based bodies rather than forward-facing geometries or ribs, which are more relevant to the present investigation. Their findings suggest that optimizing geometric features can yield significant aerodynamic benefits, aligning with the study's objective to refine rib design for superior performance in suddenly expanded flows. Further studies by M. Kavimandan et al. [19] and Saravanan et al. [20] investigated the aerothermodynamic effects of forward-facing cavities, highlighting their potential to reduce thermal loads in high-speed aerospace applications. While their research aligns with the broader goal

of enhancing aerodynamic performance, it does not directly address passive rib-based control methods.

Beyond the extensively studied passive control techniques, other innovative approaches have also been explored recently. B. Sudarshan [21] investigated the cavity's effect in the flow direction through a competing high-pressure jet combination at a Mach number M = 6. S. Mohandas et al. [22] investigated wave drag reduction on blunt bodies utilizing spikes with diverse apex geometries, demonstrating that spikes effectively alter shock formation and reduce aerodynamic drag. However, their study primarily focused on external flow aerodynamics, whereas the present research examines internal flow modification through the use of corrugated ribs. Engblom et al. [23] conducted numerical studies and tests on forward-facing cavity flows at Mach numbers M> 5, providing insights into the complex flow behavior at extreme Mach numbers. While their study provided foundational knowledge on cavity-induced pressure regulation, it did not explore passive control methods, such as ribs, which can be integrated into similar aerodynamic designs.

Huang et al. [24] conducted a parametric investigation into the reduction of heat flux and base drag using forward-facing cavities on blunt bodies. Their findings emphasized that cavity geometry is crucial in controlling aerodynamic heating and pressure fluctuations. This aligns with the present study's objective of optimizing geometric configurations for drag reduction. However, while their research examined cavity-induced drag reduction, the current study investigates the impact of rib configurations on base pressure control, addressing a gap in the literature by exploring how rib-induced vortices influence the recirculation region. Finally, Santos [25] analyzed the aerothermodynamics of rounded leading edges in hypersonic flow, accounting for real gas effects, with a focus on heat transfer and aerodynamic behavior under extreme conditions. While his work is crucial for understanding shockwave behavior and surface heating, it did not specifically address passive flow control mechanisms for drag reduction.

Khan et al. [26,27] studied the effect of the base cavity and dimple cavities on the base flows at low Mach numbers. Sajli et al. [28] numerically investigated the flow field of a non-circular cylinder at low speeds. Khan et al. [29-30] studied the effect of expansion level, as well as the favorable pressure gradient, in a suddenly expanded flow at supersonic speeds using microjets. Results show that the control in the form of tiny jets is effective when the nozzles are under-expanded. These results reiterate that whether active or passive

control methods become effective depends on the nozzles flowing under the influence of a favorable pressure gradient.

However, while the review highlights the potential of flow control techniques, it does not extensively focus on the role of ribs, particularly corrugated ribs, in mitigating base drag. This limitation highlights the need for the present study, which systematically examines the impact of corrugated ribs on base pressure enhancement at Mach unity.

The current research introduces several novel aspects of base pressure regulation. Firstly, employing corrugated ribs as a passive control mechanism remains an underexplored area, with limited studies available in the literature. This work systematically investigates the impact of rib height and placement on base pressure, providing valuable insights into the optimal design of corrugated ribs for enhancing base pressure. Secondly, this study employs advanced computational fluid dynamics (CFD) techniques, including the k-epsilon model, to account for turbulence and the finite volume method (FVM) to simulate the complex flow dynamics associated with corrugated ribs. The validation of CFD results against experimental data further enhances the credibility of this research. Lastly, the study highlights the potential environmental and energy implications of base pressure control, demonstrating that corrugated ribs could contribute to the development of more energy-efficient aerospace vehicles. By addressing the shortcomings of previous studies, the present research offers significant advancements in passive control techniques for supersonic and hypersonic flow applications.

As discussed in the preceding literature review, high-speed flows that adopt active and passive regulation appear to serve multiple purposes. In earlier studies, researchers focused on wind tunnel tests. Interestingly, every item in the collection is entirely experimental, utilizing cavities, ribs, or microjets. Nevertheless, no computational research has been conducted on passive base pressure management to determine the finer points of flow phenomena that follow flow expansion using ribs. Considering this interest, ribs with varying width-to-height ratios will be employed in this paper as a passive control technique using a computational standard turbulence model. The placement and geometry of the ribs determine the base pressure. So far, researchers have not attempted to control the base pressure using a quarter-circle rib. Hence, this study aims to assess the effectiveness of passive control in the form of a D-shaped rib with various radii at a position where the flat part of the rib faces the shear layer for different expansion levels, thereby achieving the mission requirements.

3. Computational Fluid Dynamics

a. Governing Equations

The following hypotheses are taken into consideration:

i. Turbulent flow is considered because of the turbulent viscous dissipation effects.

ii. The fluid's viscosity varies with temperature and is compressible.

iii. At atmospheric pressure, the flow exits the duct.

iv. While reviewing the literature, we found that the internal flow k-ε turbulence model yields the best results, as it provides reasonably accurate predictions. Sutherland's three-coefficient viscosity model is expressed as follows:

$$\mu' = \mu'_o \left(\frac{T_a}{T_{a,o}}\right)^{3/2} \frac{T_{a,o}+S\prime}{T_a+S\prime} \tag{1}$$

The reference viscosity value in kg/m-s is denoted as μ'_o, where μ' represents the viscosity. T_a denotes static temperature; K represents the temperature of a standard reference, and S' is the temperature-dependent Sutherland constant. Three-dimensional continuity equation for compressible flow:

The equation for mass balance is as follows:

$$\frac{\partial \rho}{\partial t} + \underline{\nabla} \cdot (\rho \underline{V}) = 0 \tag{2}$$

Where the fluid's velocity is denoted by V. The equation for momentum balance is:

$$\frac{\partial}{\partial t}(\rho \underline{V}) + \underline{\nabla} \cdot (\rho \underline{V}\underline{V}) + \underline{\nabla} p = \underline{\nabla} \cdot \left[2\mu (\underline{\nabla V})_o^s\right] + \underline{\nabla} \cdot (\tau_{=Re}) \tag{3}$$

Where $(\underline{\nabla V})_o^s = (\underline{\nabla V})^s - \frac{1}{3}(\underline{\nabla} \cdot \underline{V})\underline{I}$, $(\underline{\nabla V})^s = \frac{\underline{\nabla V} + \underline{\nabla V}^T}{2}$ and $\tau_{=Re}$ is the turbulent stress tensor. The formulae for total energy are as follows:

$$\frac{\partial}{\partial t}\left[\rho\left(\frac{1}{2}V^2 + u_{int}\right)\right] + \underline{\nabla}\left[\rho\left(\frac{1}{2}V^2 + u_{int}\right)\underline{V}\right] = \underline{\nabla}\left(\lambda \underline{\nabla} T - p\underline{V} + 2\mu \underline{V} \cdot (\underline{\nabla V})_o^s + \underline{V} \cdot \tau_{=Re}\right) \tag{4}$$

Where u_{int} is the internal energy, and λ is the thermal conductivity. Many internal flow simulations use the k-epsilon turbulence model due to its affordability, resilience, and sufficient accuracy. The Ansys Fluent program incorporates the k-epsilon (ε) turbulence model used in this research. The K-equation allowed us to calculate the turbulent kinetic energy.

$$\frac{\partial}{\partial t}(\rho k) + \underline{\nabla} \cdot (\rho \underline{V} k) = \underline{\nabla} \cdot \left[(\mu + \frac{\mu_t}{\sigma_k})(\underline{\nabla} k)\right] - \rho\varepsilon + M_x \tag{5}$$

The turbulent kinetic energy dissipation rate is denoted by ε, the turbulent Prandtl number

is σ-k, and the word Mx is the turbulence generation. Precisely, the dissipation (or (-equation)) is controlled by,

$$\frac{\partial(\rho\varepsilon)}{\partial t} = -\underline{\nabla}\cdot\left(\rho\varepsilon\vec{V}\right) + \underline{\nabla}\cdot\left[\left(\mu + \frac{\mu_T}{\sigma_\varepsilon}\right)\nabla\varepsilon\right] - C_1 f_1\left(\frac{\varepsilon}{k}\right)M - C_2 f_2\frac{\varepsilon^2}{k} \quad (6)$$

where $\mu_t = \rho f_\mu C_\mu k^2/\varepsilon$ denotes turbulent viscosity, and the arbitrary constants are denoted as $\overline{C_\mu} = 0.09$, $\overline{C_1} = 1.44$, $\overline{C_2} = 1.92$, $\overline{f_\mu} = 1$, $\sigma_k = 1.0$ and $\sigma_\varepsilon = 1.3$.

4. Finite Volume Method

4.1 Geometry and Modelling

The finite volume technique (FVM) was employed to delve further into this investigation. The CFD simulation utilized the ANSYS FLUENT 2024/R2 software to evaluate the fluid flow through the nozzle. We are examining the impact of the D-shape of the rib using a passive control method. The two orientations of the D-shape rib are shown in Figure 1.

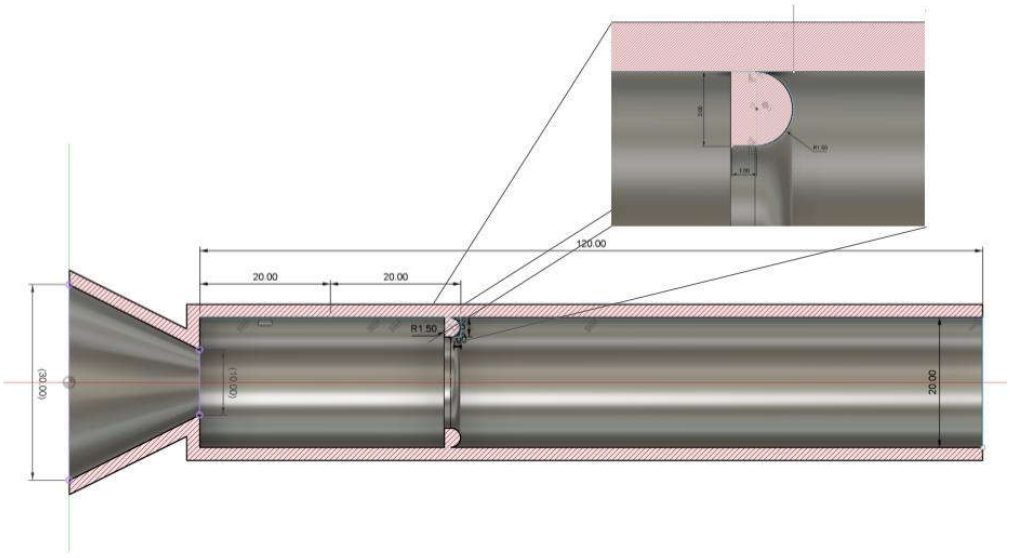

Fig. 1 Nozzle and Duct Assembly with D-shaped Rib

4.2 Meshing and Boundary Conditions

A crucial part of the CFD process is meshing. By choosing the free-face mesh type, the 2D model is of the structured mesh type in this case. Elements were assigned sizes according to the length of each line (edge) when the constructed structured mesh type was used. The lines were utilized to apply the element size, and elements with identical forms were created using

face meshing. The mesh independence check is done. Figure 2 below shows the mesh's element type and size tested during the mesh independence check. Mesh independence test for duct 20 mm – without rib (L/D = 6). Different element sizes and their properties are based on the same geometry model.

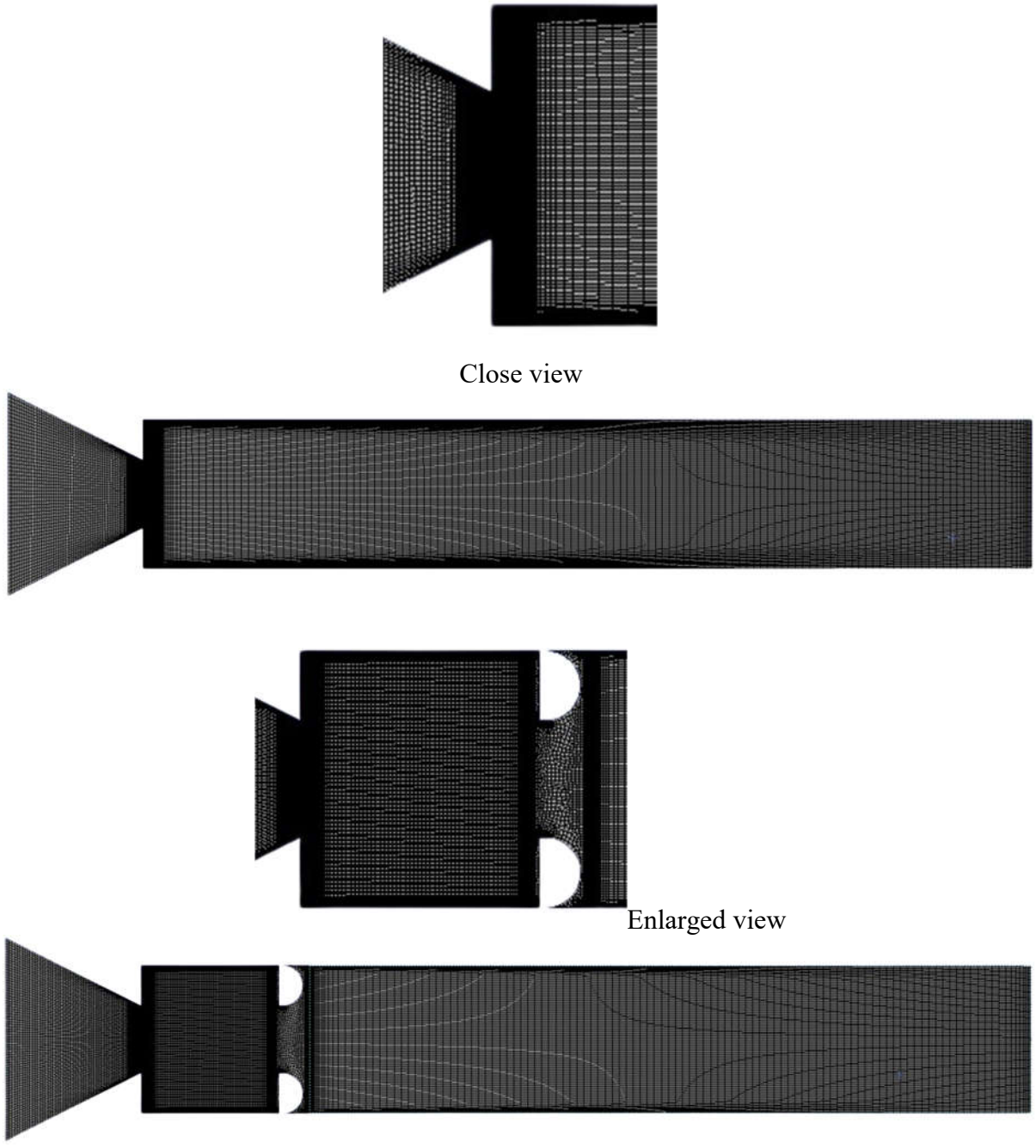

(b)

Figure 2: Mesh model (a) without control (b) with control orientation

4.3 Assumptions and Fluid Properties

Assumptions are made to replicate the flow activities in the precise physical environment. Appropriate mathematical and numerical models are selected to simplify the governing equations.

To solve the governing equations simultaneously, numerical modeling requires selecting the appropriate mathematical models, including the governing equations, boundary conditions, mesh quality, and numerical method. Despite its limitations in accurately representing physical phenomena, the computational method has been trusted for decades and offers sufficient insight into flow behavior. As a result, this calls for careful consideration of elements that closely resemble the flow behavior. This study pinpoints the presumptions that jeopardize the precise physical state. The following are the assumptions and characteristics covered in this study:

i. The flow is assumed to be a steady 2D flow because the geometry is symmetric. Hence, the assumption that the flow is 2-D is justified.
ii. The density of the air is variable as the flow is compressible. The inlet pressure is the gauge pressure at that Mach number and NPR, and at the outlet of the duct, the gauge pressure is zero.
iii. Turbulent flow significantly impacts turbulent viscous dissipation at a given flow velocity, so it is considered.
iv. The viscosity of the fluid is dependent on temperature.
v. At standard atmospheric pressure, the flows leave the duct. At normal ambient pressure, they do not.

Since the flow via the nozzle is considered turbulent, the compressible flow field is represented by the k-epsilon standard model. The subsequent equations most appropriately characterize the turbulent flow.

4.4 ***Validation of Experimental Model***

The ANSYS Workbench program utilized fluid flow (Fluent) analytical techniques throughout the computational fluid dynamics (CFD) procedure. The model was generated via a Design Modeler. Figure 3 depicts a converging nozzle that abruptly widens into a duct with five ribs. Rathakrishnan [25] experimental setup, the dimensions of the convergent-divergent nozzle with a suddenly expanded duct are as stated below.

Table 1

The geometries of the validation model

Parameters	Dimensions
Nozzle inlet diameter	30 mm
Nozzle outlet diameter	10 mm
Duct diameter	22 mm
Duct length	Varies from 1D to 6D
Converging length	20 mm
Rib width	3 mm
Rib height	Varies from 1mm to 3mm

Figure 3 illustrates the base pressure ratio data from current and earlier studies [25]. The experimental values were denoted by dotted lines, while the simulation results obtained using ANSYS Fluent were represented by straight lines. The present numerical analysis exhibited a percentage discrepancy of less than 10% compared to the previous experimental study. Consequently, the current work met the criteria for acceptability. The curves exhibited a consistent pattern, with each point closely following the next. As a result, based on the table and graph described before, the validation of the current work was successful.

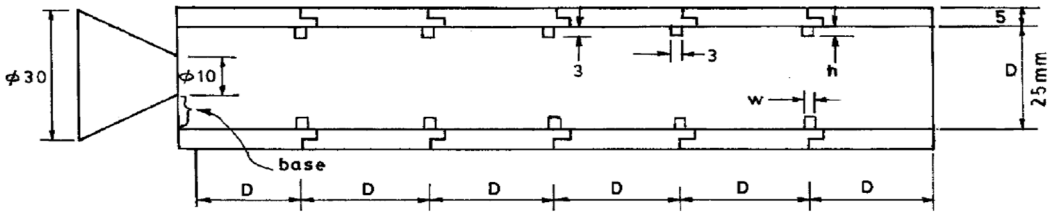

Figure 3: Duct with five ribs used in an experimental study [1]

According to Rathakrishnan [1], the prior work was performed at aspect ratios of 3:3, 3:2, and 3:1; an area ratio of 6.25; L/D ranging from 1 to 6; pressure ratios of 1.141, 1.295, 1.550, 1.707, and 2.458; and nozzle exit Mach numbers of 0.44, 0.62, 0.82, 0.91, and 1.0. However, in a prior publication by Rathakrishnan [1], the result from Figure 4 with NPR (P_{01}/P_a) of 2.458 and models with control in the form of ribs with aspect ratios of 3:2 and 3:3 was chosen for comparison with the current work. The simulation is supported by Rathakrishnan's [1] experimental work, which used five ribs positioned at equidistant intervals in the duct, as illustrated in Figure 4. The results of base pressure fluctuation with NPR of 2.458 and L/D

ranging from 2 to 6 are obtained. The study is repeated to validate the numerical results of a model with control over different rib aspect ratios [1].

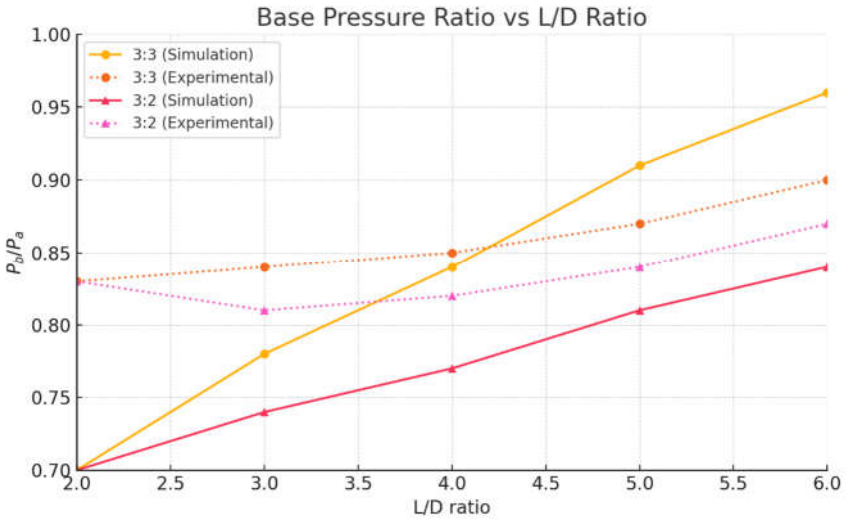

Figure 4: Validation of previous work by Rathakrishnan [38]

4.5 Mesh Independence Study

Table 2 presents data from a mesh independence study, a crucial step in computational simulations that ensures the results remain consistent regardless of the mesh refinement level. The element sizes range from coarse to fine, with corresponding node and element counts for each mesh configuration. As the mesh becomes finer, the number of nodes and elements increases significantly, from 1,284 nodes and 1,145 elements in the coarsest mesh to 1,354,262 nodes and 1,351,303 elements in the finest mesh. This study aims to determine the optimal mesh size for accurate simulations without unnecessary computational expense. The table shows a notable increase in nodes and elements as the mesh is refined. The coarsest mesh has relatively few nodes and elements, resulting in a lower computational cost but potentially less accuracy. Conversely, the finest mesh offers the highest resolution at the expense of significant computational resources. The medium and fine meshes provide intermediate levels of refinement, offering a balance between accuracy and efficiency.

Table 2: Mesh independence study

Element size	Coarsest	Coarse	Medium 1	Medium 2	Fine	Finer	Finest
Nodes	2703	5573	18053	35486	264734	762769	3885169
Elements	2500	5286	17577	34838	263101	760026	3879157

Based on the trends in node and element numbers, the finest mesh will likely produce the most accurate results (Figure 5). However, continuing to refine the mesh beyond a certain point may offer diminishing returns in terms of accuracy while significantly increasing computational

time. A critical assessment of this table would suggest that the "Fine" or "Finer" mesh configurations may represent the best balance between accuracy and computational efficiency. These configurations substantially increase the number of nodes and elements compared to the medium meshes, without reaching the computational expense of the finest mesh. If the simulation results do not change significantly between the fine and finest meshes, further refinement of the finest mesh is unnecessary, as it would only increase computational time without added benefit. Thus, the fine or finer mesh sizes are likely the best choices for further simulation.

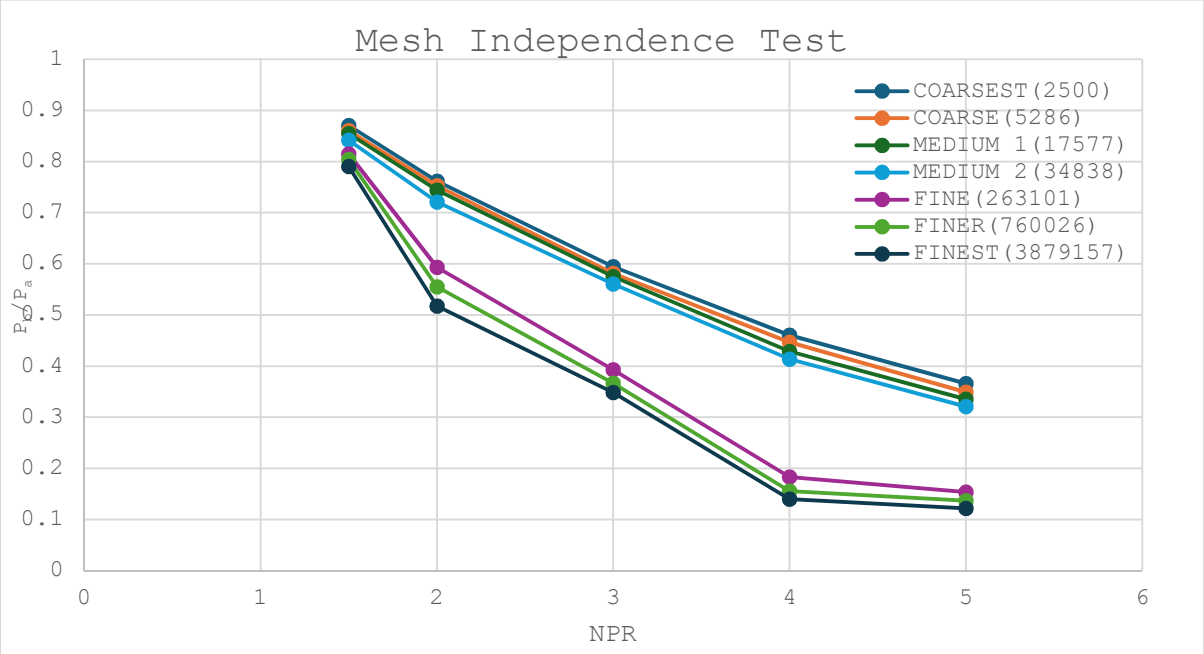

Figure 5: Results of mesh check

5. Results and Discussions:

Before examining the findings, it would be helpful to understand the mechanics underlying the abrupt increase in the flow field. Figure 6 illustrates how the boundary layer at the nozzle exit forms a free shear layer for subsonic flows and meets the expanded duct wall downstream.

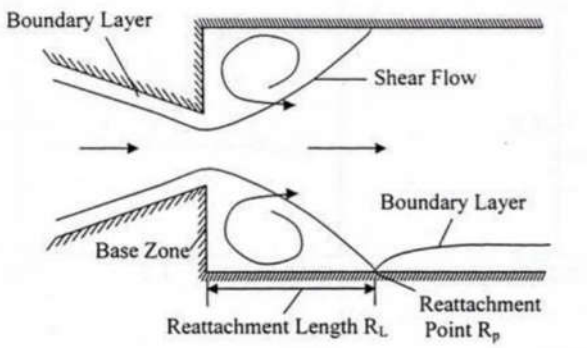

Fig. 6 Sudden Expansion Flow Field

The reattachment point is the location where the flow attaches. Reattachment length is the distance between the base and the point of reattachment. One or more vortices will be positioned between the base, the reattachment point, and the edge of the free shear layer. The first, strong vortex near the base is called the primary vortex. That moves fluid from the base to the main flow on the other side of the free shear layer edge. There is low pressure at the base due to this pumping motion. The pumping, however, also becomes periodic since vortex shedding is a periodic event. The base pressure varies as a result of this. Nonetheless, it was found that the base pressure variations were often minimal and could be expressed as a mean value. Oscillatory flow occurs throughout the duct due to the periodicity of the vortex motion. There are several flow and geometrical parameter combinations where the oscillations can get terrible. To adjust the primary vortex strength, the reattachment, and the flow Mach number significantly impact the suction at the base and the flow oscillations in the duct.

5.1 Control with Rib Orientation When the shear layer is facing the Flat surface of the Rib

Figure 12 shows the orientation of the rib as 2. In this arrangement, the flat part of the rib faces the base region, and the curved part is downstream or at the aft of the rib. In the previous case, as shown in Fig. 6, the curved part of the rib faces the base region, and the vertically flat part is downstream. In this study, the ribs were positioned at two different orientations to determine their effectiveness in both cases. As seen in Fig. 7, the shear layer, upon exiting the nozzle, allowed it to expand to a larger diameter of 20 mm, from the 10 mm converging nozzle exit diameter. In the following section, we will discuss the efficacy of the ribs for this orientation. In Fig. 7, this orientation is expected to result in better efficiency of the passive control.

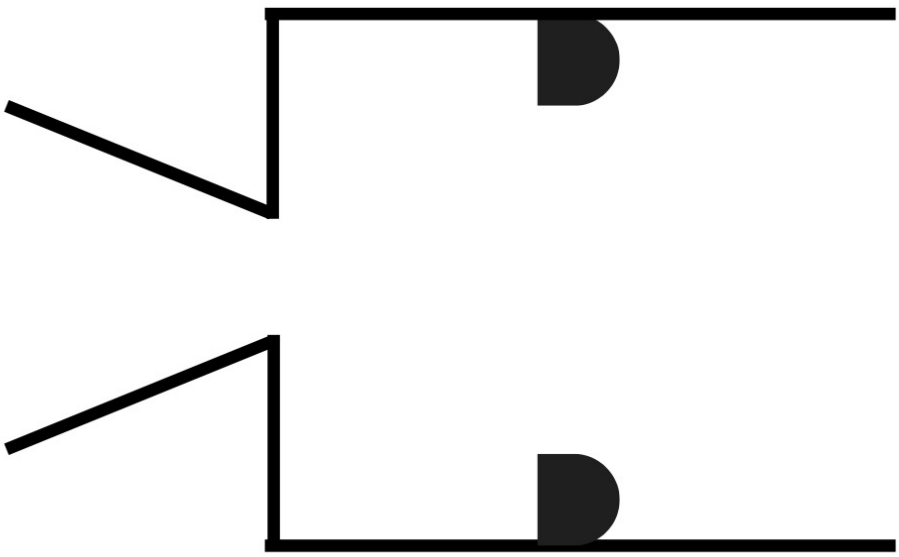

u

Figure 7: Converging Nozzle and Duct Assembly with D-shape Rib for Orientation 2

5.2 Base Pressure Results for Rib Location at L/D = 0.5

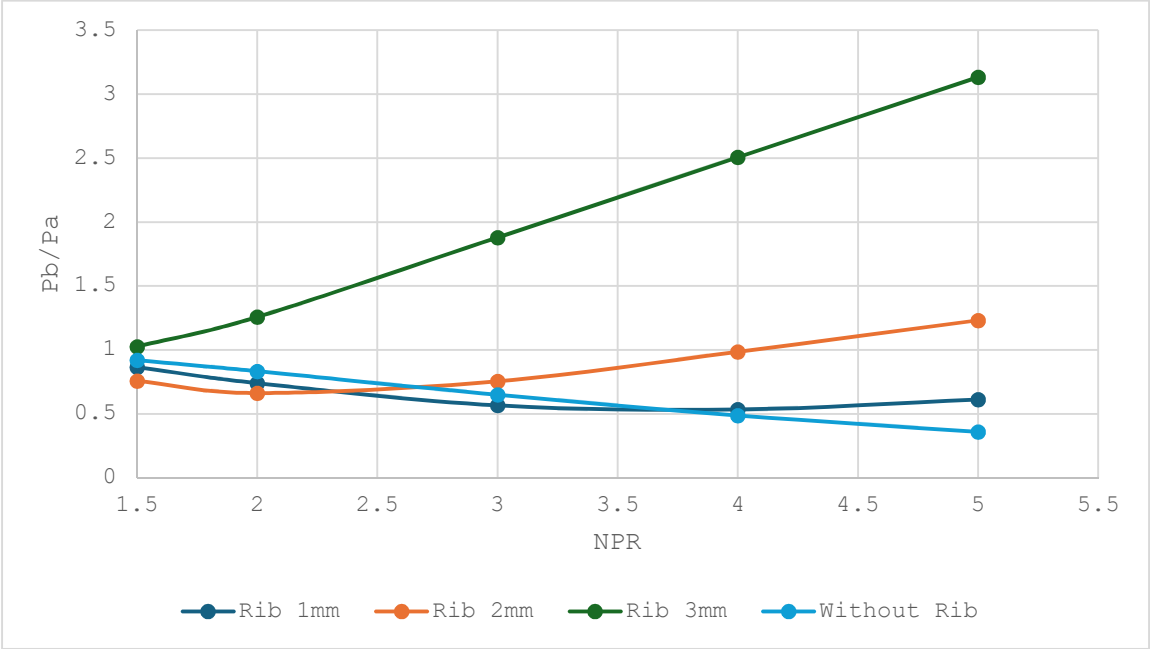

(a) L/D = 1

The findings of this study for orientation two are shown in Figs. 8 (a) to (f), where the flat surface of the rib will interact with the shear layer and is expected to increase the base pressure as compared to the orientation where the shear layer interacts with the curved part of the rib. Fig. 8(a) shows that the pattern of the base pressure is getting reversed for rib radii of 0.5 mm and 1 mm. The base pressure decreases for nozzle pressure ratios (NPRs) ranging from 1.5 to 2 for rib radii of 1

and 0.5, as well as for NPRs between 4 and 5. Similarly, there is an increasing trend for rib radii of 0.5 and 1mm for NPRs in the range of 1.5 to 3.5 and 2 to 5. This trend in base pressure is not considered, as the rib is located at L/D = 0.5, and the flow is in transition, having not yet stabilized.

Similar trends in the base pressure are observed for other duct lengths, namely L/D = 2 to 6. There are marginal variations in the magnitude of the base pressure due to the influence of the ambient atmospheric pressure and the duct L/D ratio.

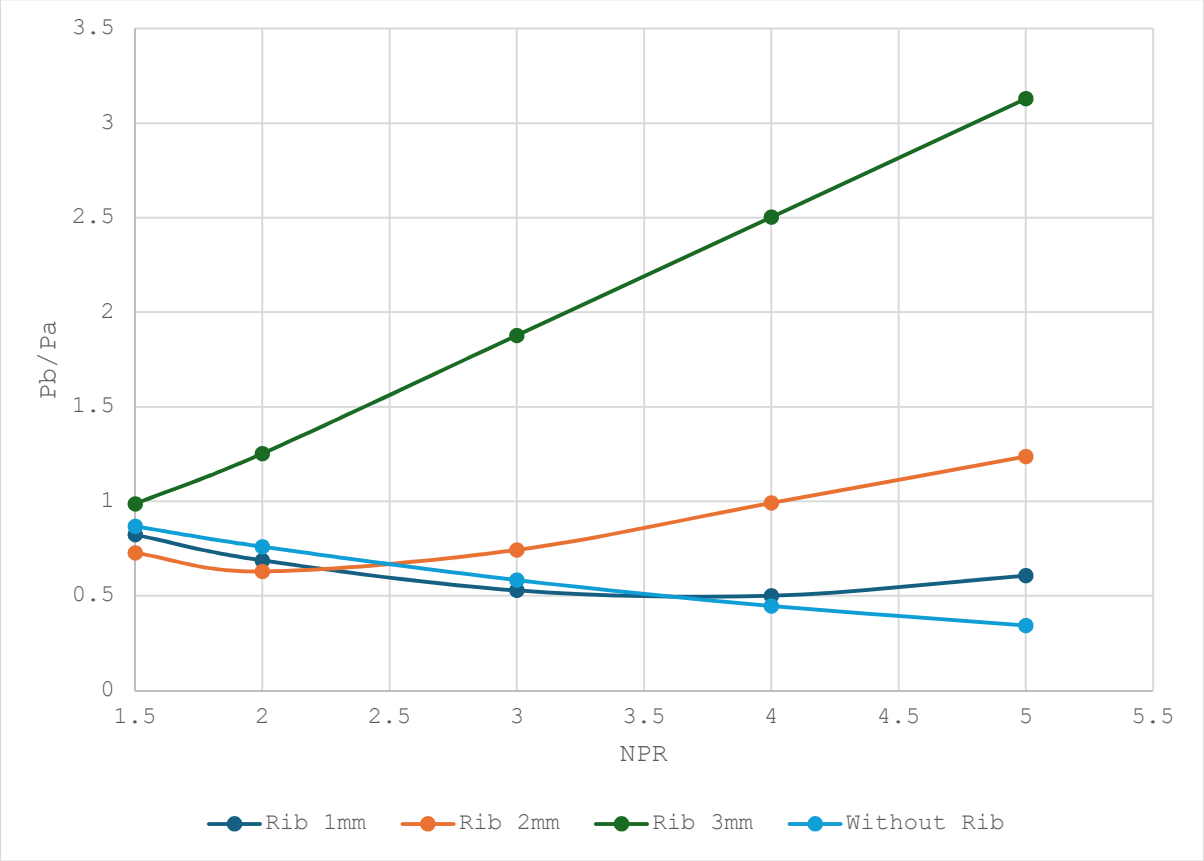

(b) L/D = 2

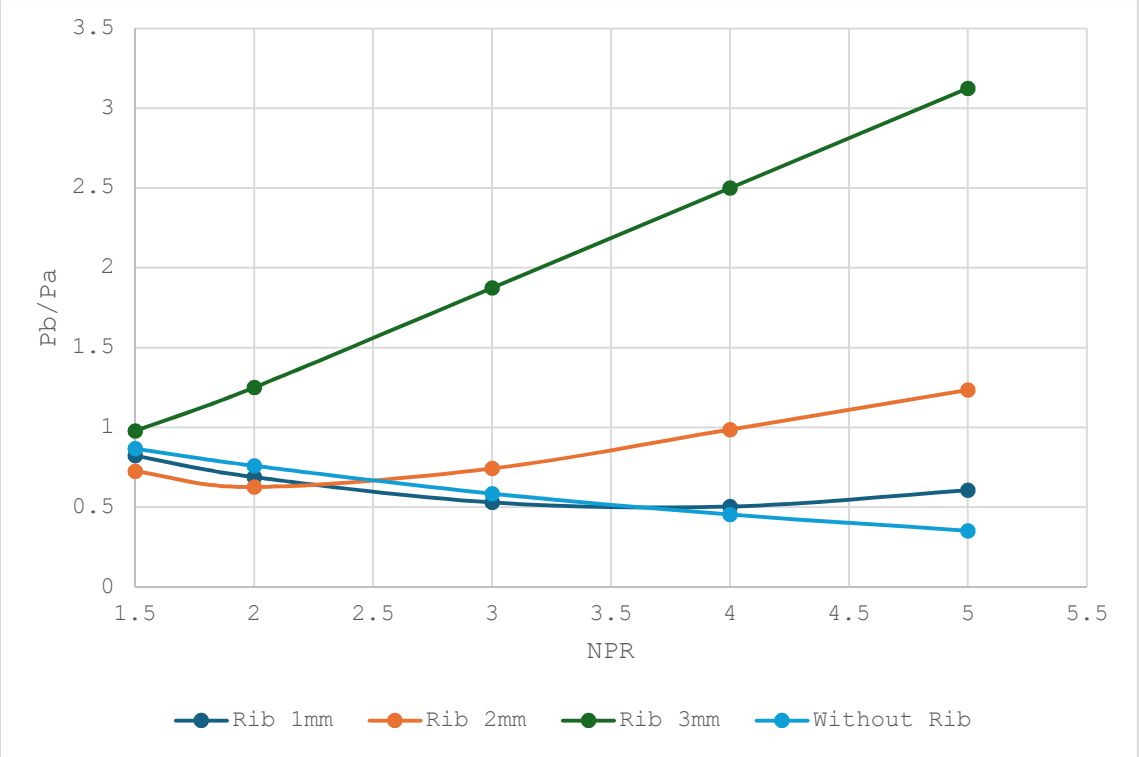
3.5
3
2.5
2
1.5
1
0.5
0
Pb/Pa
1.5
2
2.5
3
3.5
4
4.5
5
5.5
NPR
Rib 1mm
Rib 2mm
Rib 3mm
Without Rib

(c) L/D = 3

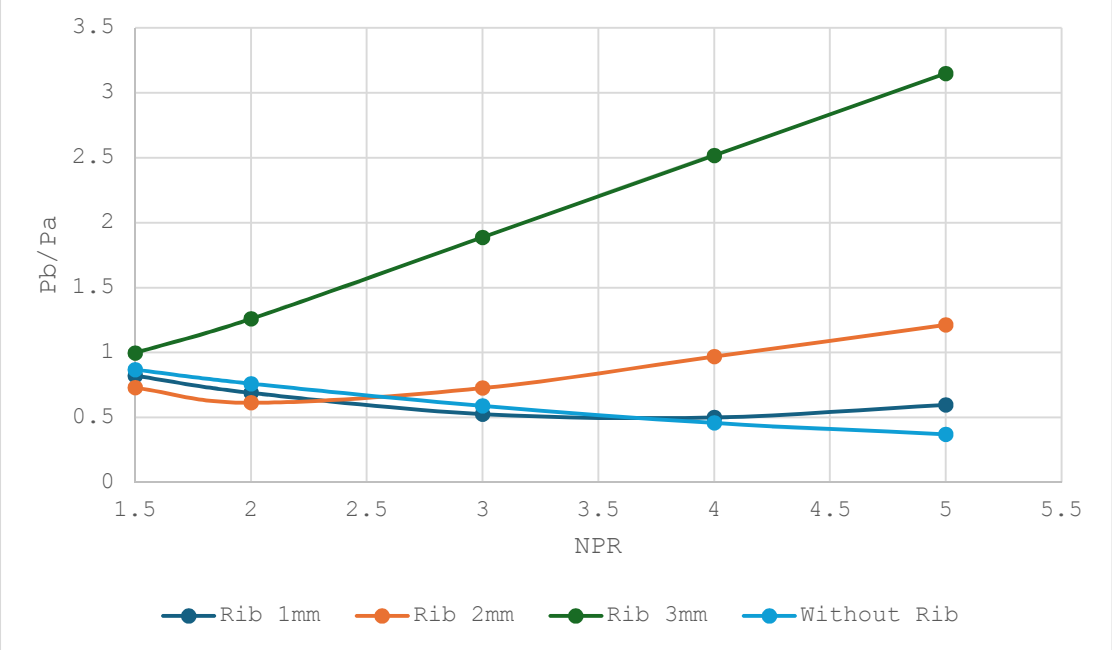
3.5
3
2.5
2
1.5
1
0.5
0
Pb/Pa
1.5
2
2.5
3
3.5
4
4.5
5
5.5
NPR
Rib 1mm
Rib 2mm
Rib 3mm
Without Rib

(d) L/D = 4

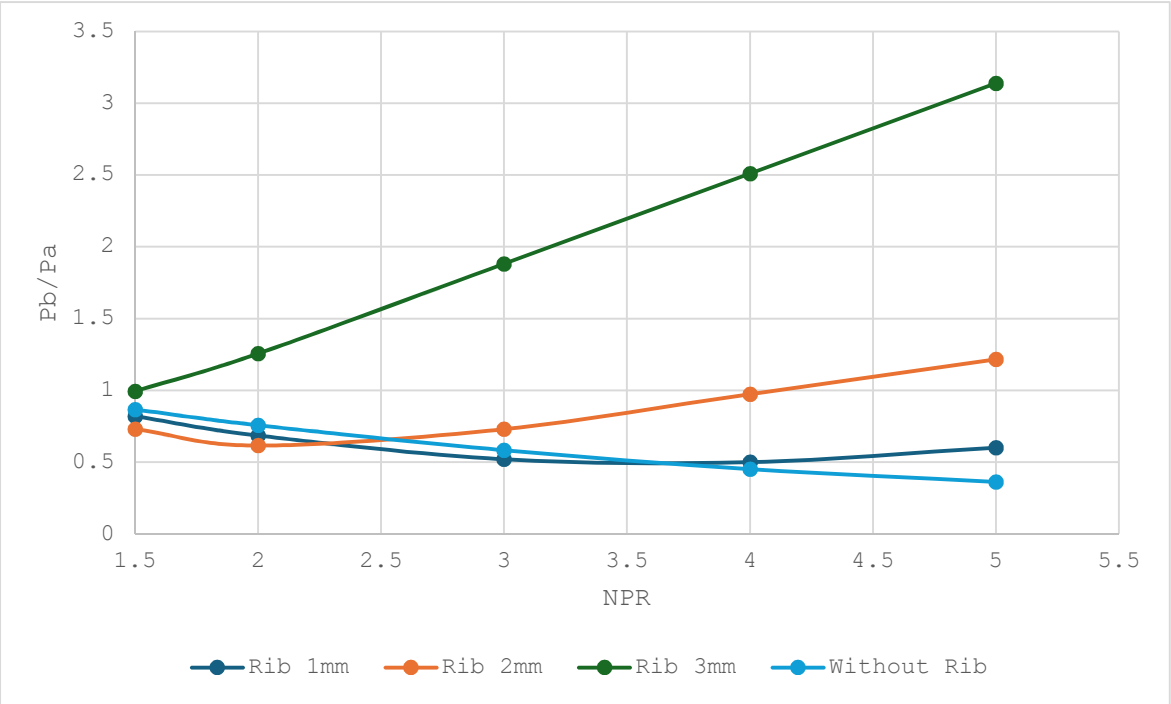

(e) L/D = 5

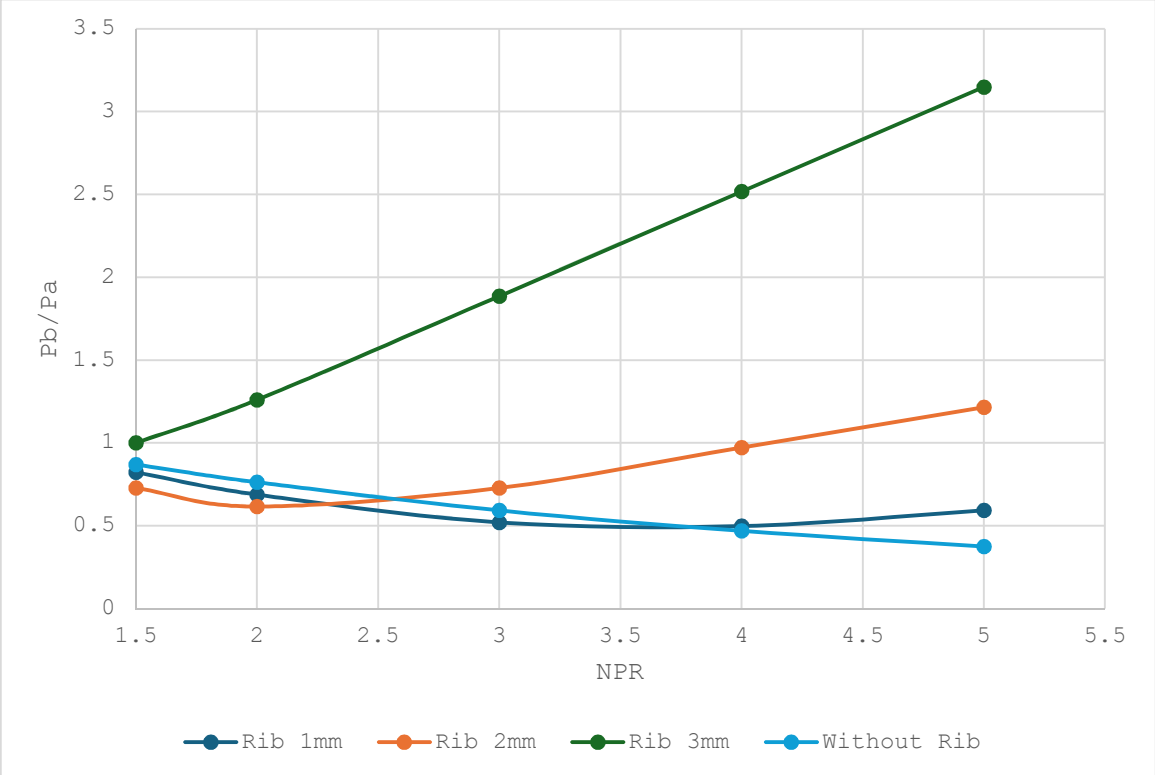

(f) L/D = 6

Fig. 8 Base Pressure Vs. NPR for numerous Duct segments

5.3 Base Pressure Results for Rib Location at L/D = 1.0

When the rib is located at L/D = 1, the findings of this study are shown in Figures 9 (a) to (e) for various NPRs and duct lengths. Fig. 9(a) presents the outcomes of the present study for a duct with L/D = 2. When we compare the base pressure results from the previous case, where the rib was placed at L/D = 0.5. As discussed earlier, when the rib is placed at L/D = 0.5, the separated flow is in transition and has not yet stabilized. Our apprehension is confirmed when we examine the base pressure results for the rib location at L/D = 1. The pattern of the results is remarkably different, as expected.

The figure shows that the control becomes effective for a rib radius of 0.5 mm, and the base increases nearly fifty percent compared to the case without ribs. In the case of rib radii of 1 mm and 1.5 mm, the declining trend is absent for the 1.5 mm rib, and for the 1mm rib, the decreasing trend is arrested once the flow is choked. However, the base pressure's magnitude is higher for a higher radius than the rib's lower radius.

Similar results are seen for other duct sizes, namely L/D = 3, 4, 5, and 6. For all these duct sizes, the base pressure values are nearly the same, with minor variations in the magnitude of the base pressure due to the influence of ambient atmospheric pressure.

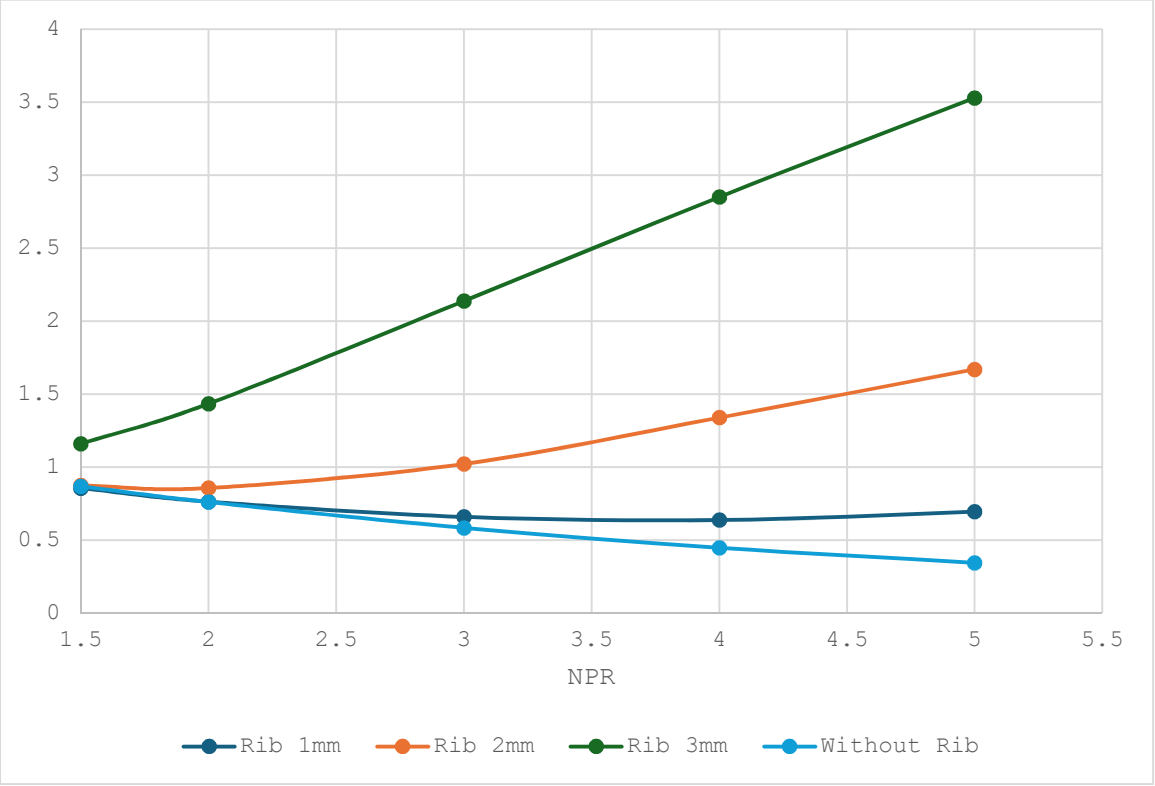

(a) L/D = 2

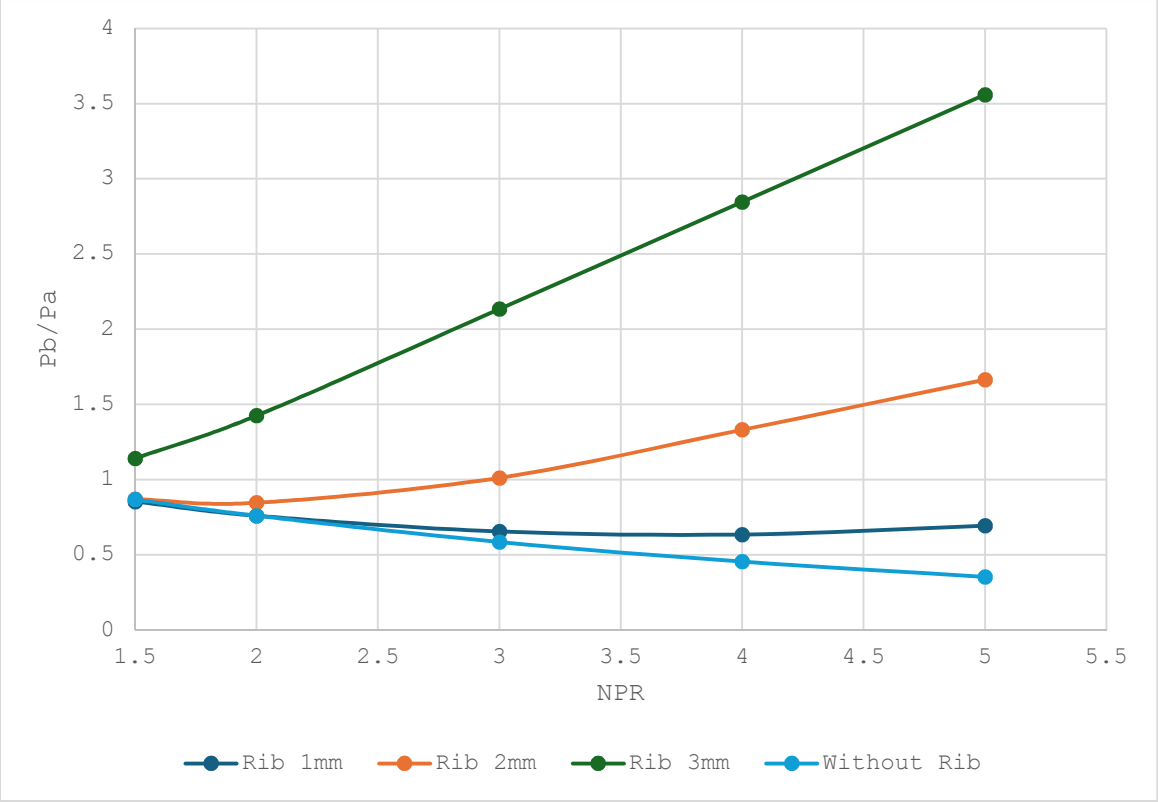
Pb/Pa
NPR
Rib 1mm
Rib 2mm
Rib 3mm
Without Rib

(b) L/D = 3

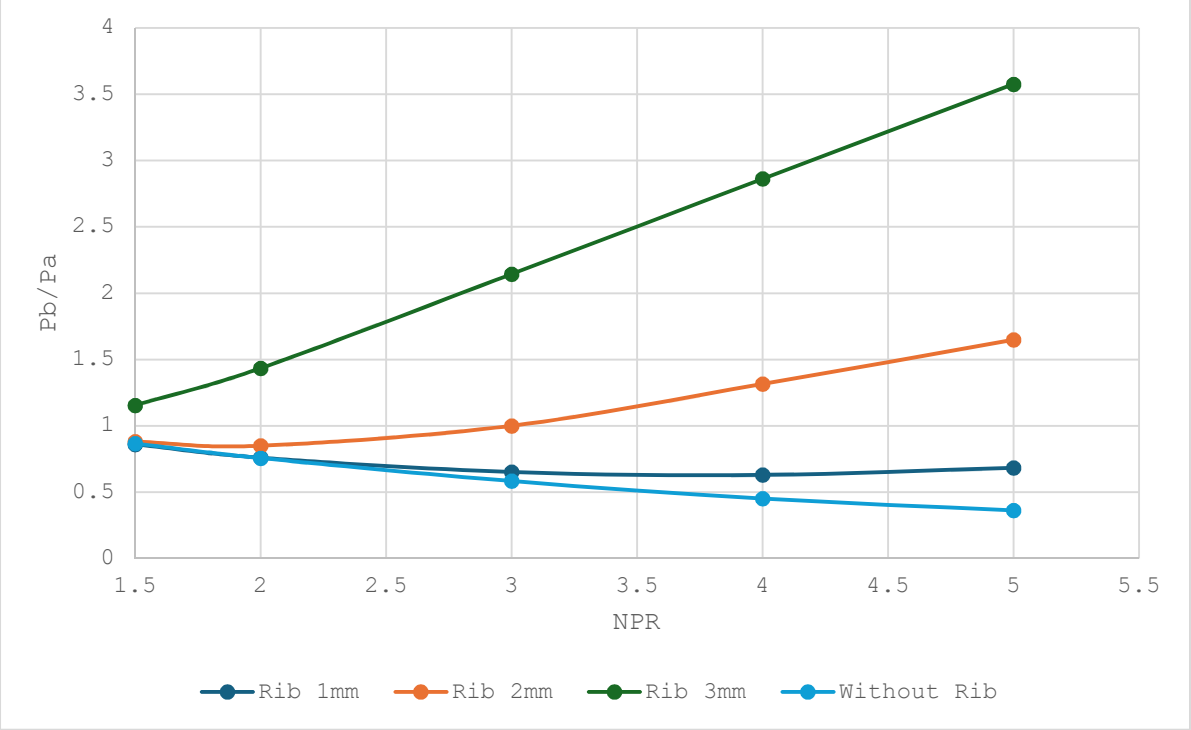
Pb/Pa
NPR
Rib 1mm
Rib 2mm
Rib 3mm
Without Rib

(c) L/D = 4

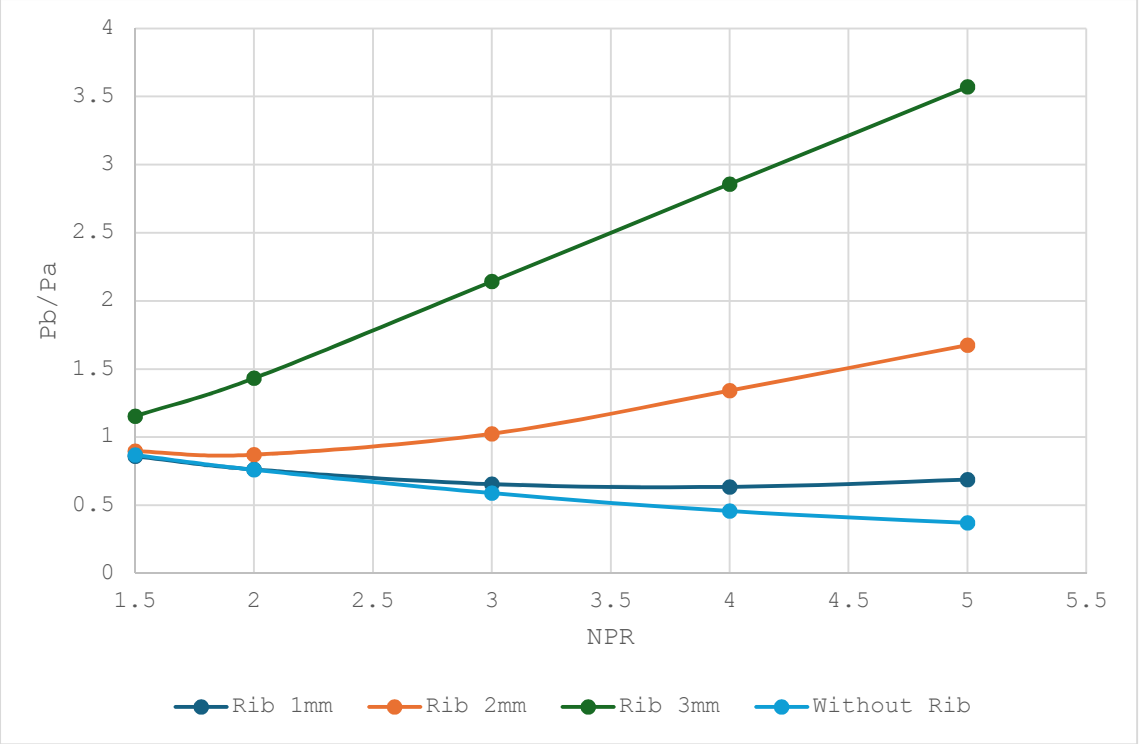

(d) L/D = 5

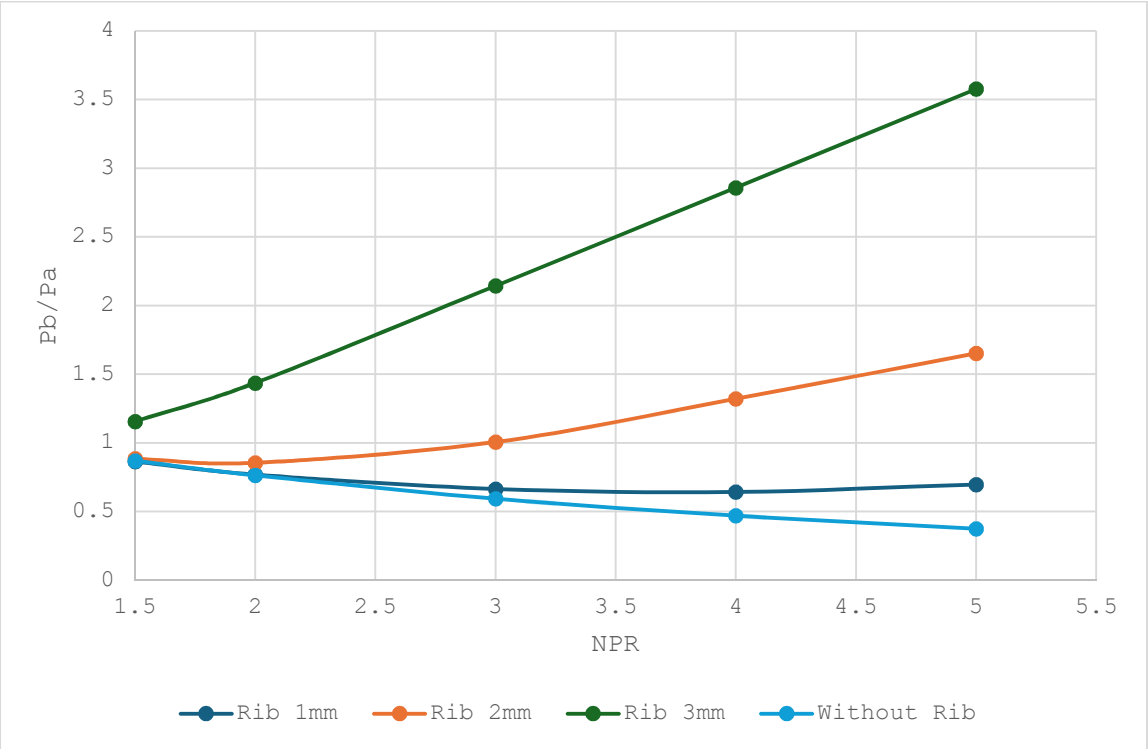

(e) L/D = 6

Fig. 9 Base Pressure Vs. NPR for numerous Duct segments

5.4 Base Pressure Results for Rib Location at L/D = 1.5

When the rib is placed at L/D = 1.5, the study's outcomes are presented in Figures 10(a) to (e) for various duct sizes and levels of expansion. Figure 10(a) shows that a considerable change in the magnitude of the base pressure is found, which is more substantial for rib radii of 1 mm and 1.5 mm. There is a slight increase in the base pressure for a 0.5 mm rib radius. These changes are attributed to the rib's location, which appears to be close to the reattachment point of the dividing streamline.

When we examine the base pressure results for other higher duct lengths, we find that their magnitude is almost the same, except for nominal changes in base pressure due to variations in duct sizes and the impact of ambient atmospheric pressure.

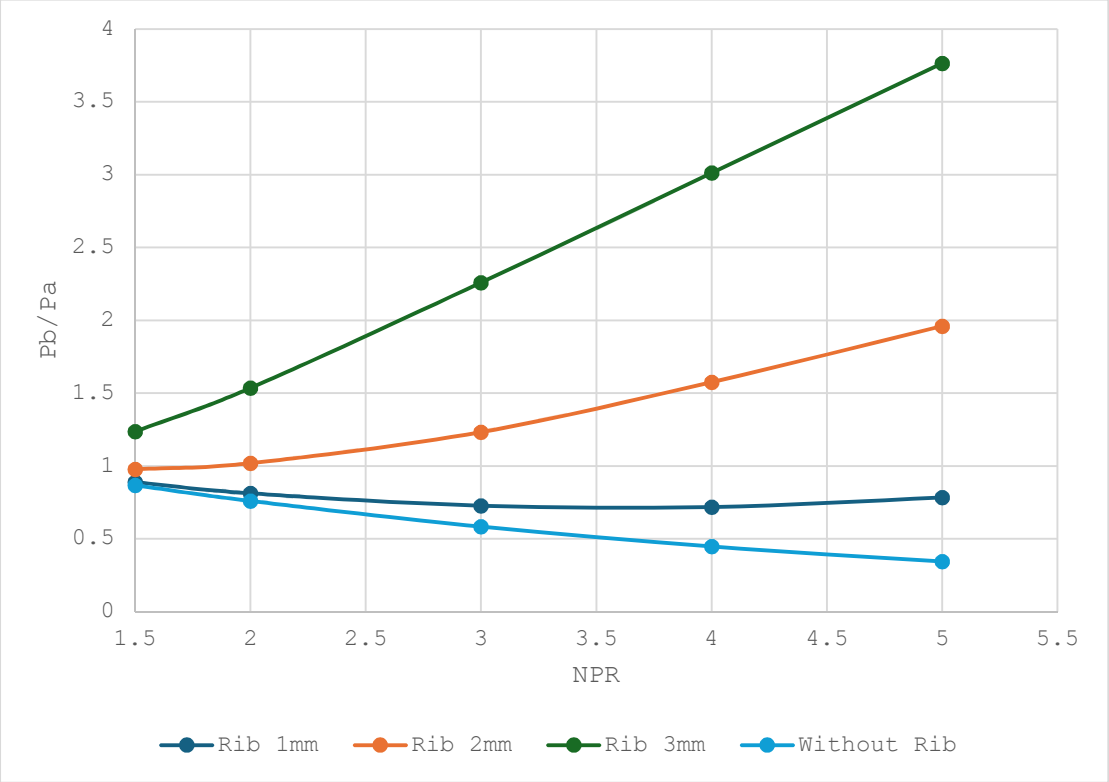

(a) L/D = 2

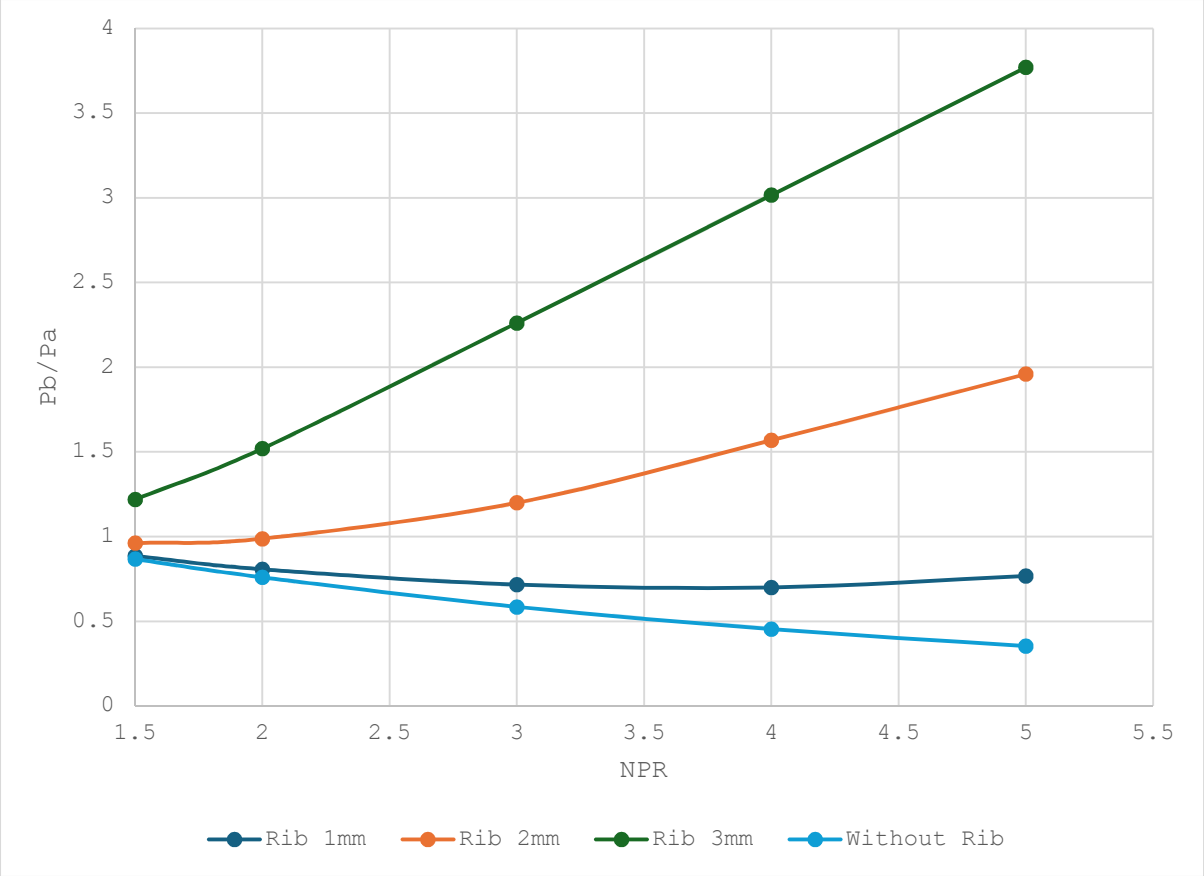
Pb/Pa
NPR
Rib 1mm
Rib 2mm
Rib 3mm
Without Rib

(b) L/D = 3

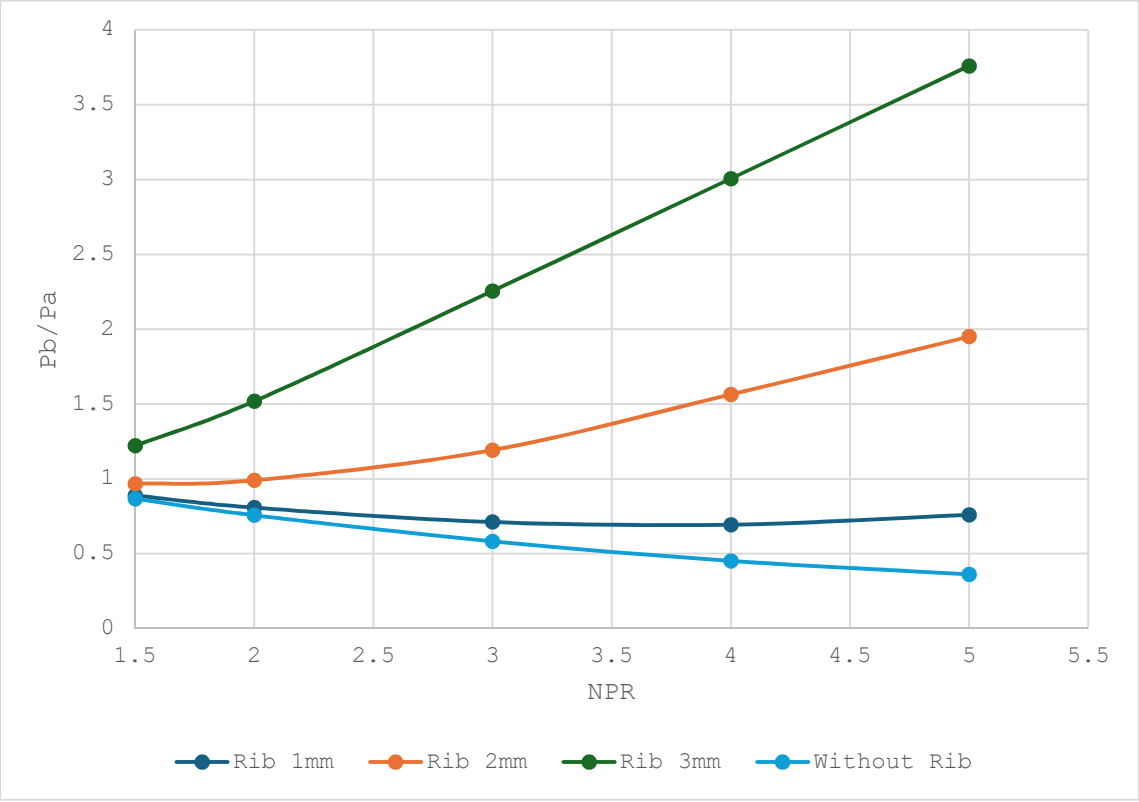
Pb/Pa
NPR
Rib 1mm
Rib 2mm
Rib 3mm
Without Rib

(c) L/D = 4

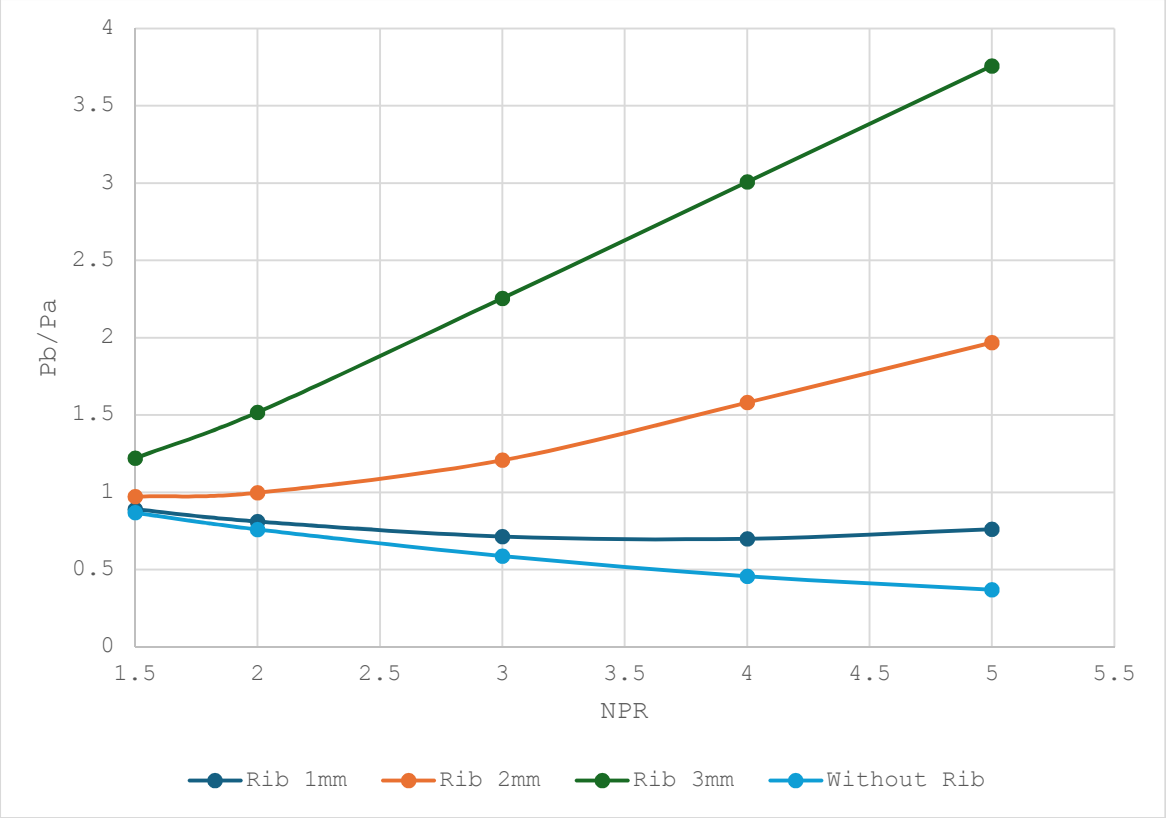

(d) L/D = 5

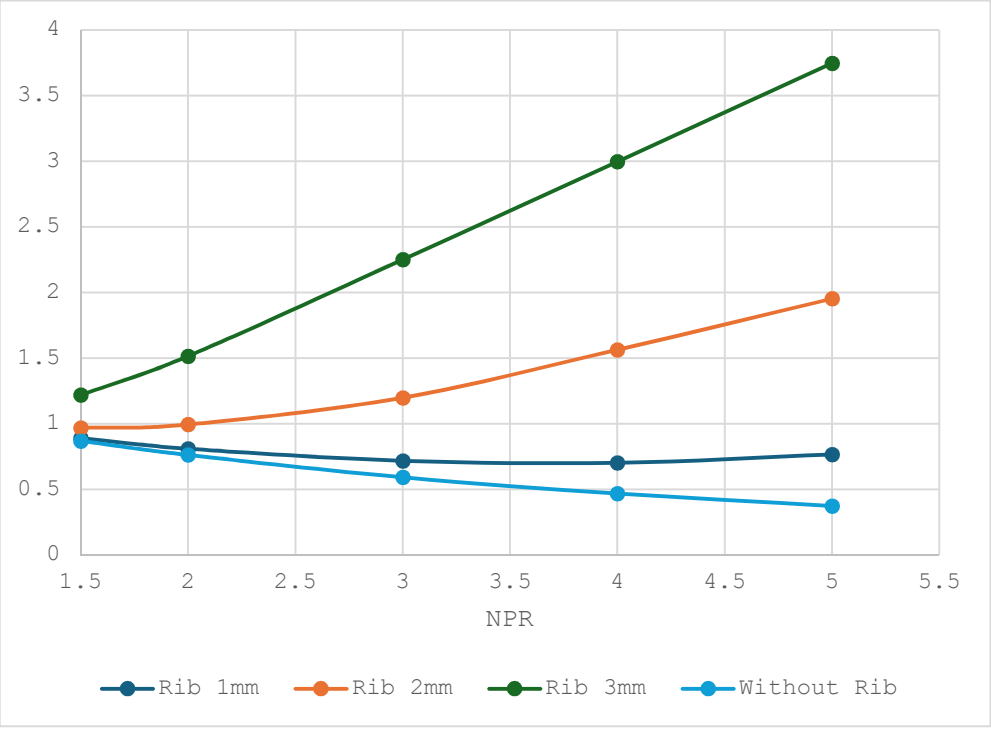

(e) L/D = 6

Fig. 10 Base Pressure Vs. NPR for numerous Duct segments

5.5 Base Pressure Results for Rib Location at L/D = 2.0

When the rib is located at L/D = 2, the base pressure resulting from this study is illustrated in Figures 11(a) to (d) for various duct sizes and nozzle pressure ratios. As discussed earlier, for a duct diameter of 20 mm, the reattachment length appears to be approximately L/D = 1 to 1.5. Once the flow is attached to the wall and the passive control mechanism is also located within the reattachment point, further shifting the rib location downstream will not result in a considerable gain in base pressure. The base pressure results are to be analyzed, taking into account these factors.

As already mentioned, the base pressure values do not change much due to increased duct length from L/D = 3 to 6. Marginal changes, if any, are caused by the shock wave interactions with the duct wall, secondary vortices generated from the rib's sharp corner, and the impact of back pressure.

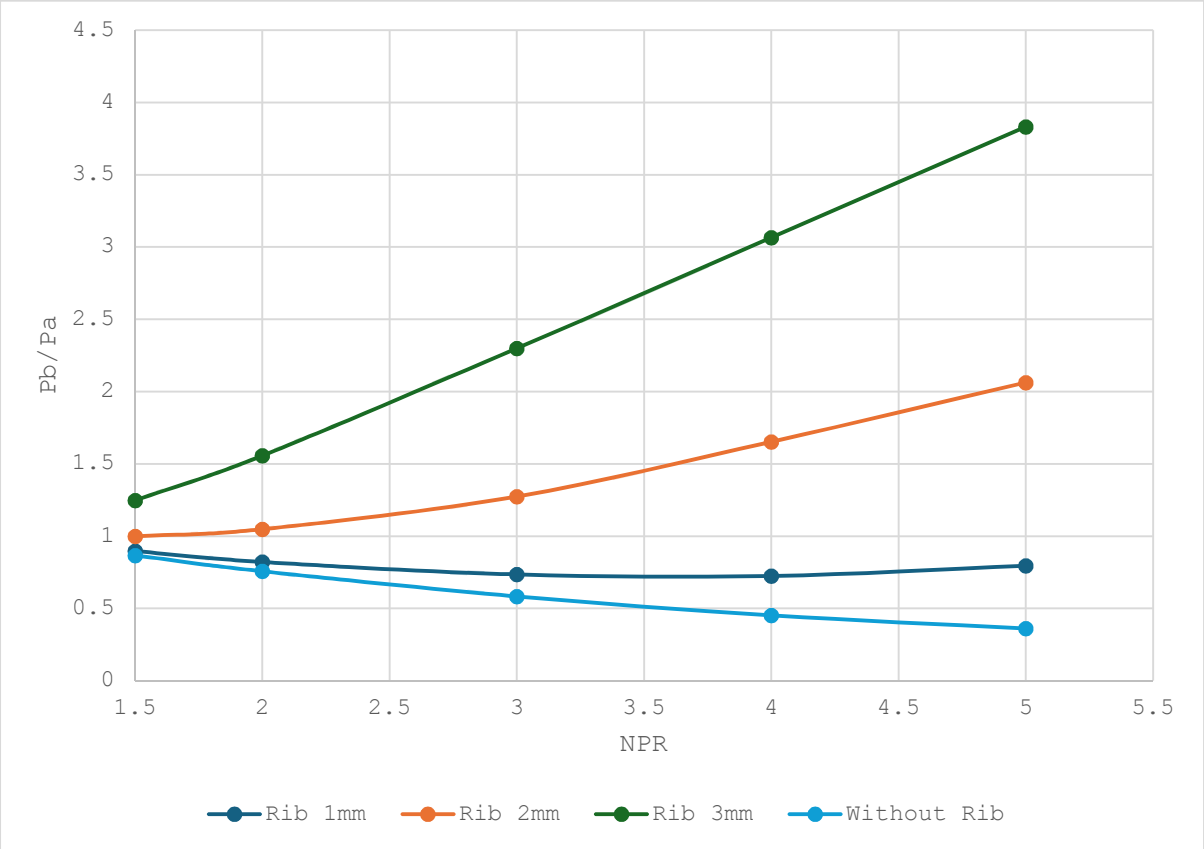

(a) L/D = 3

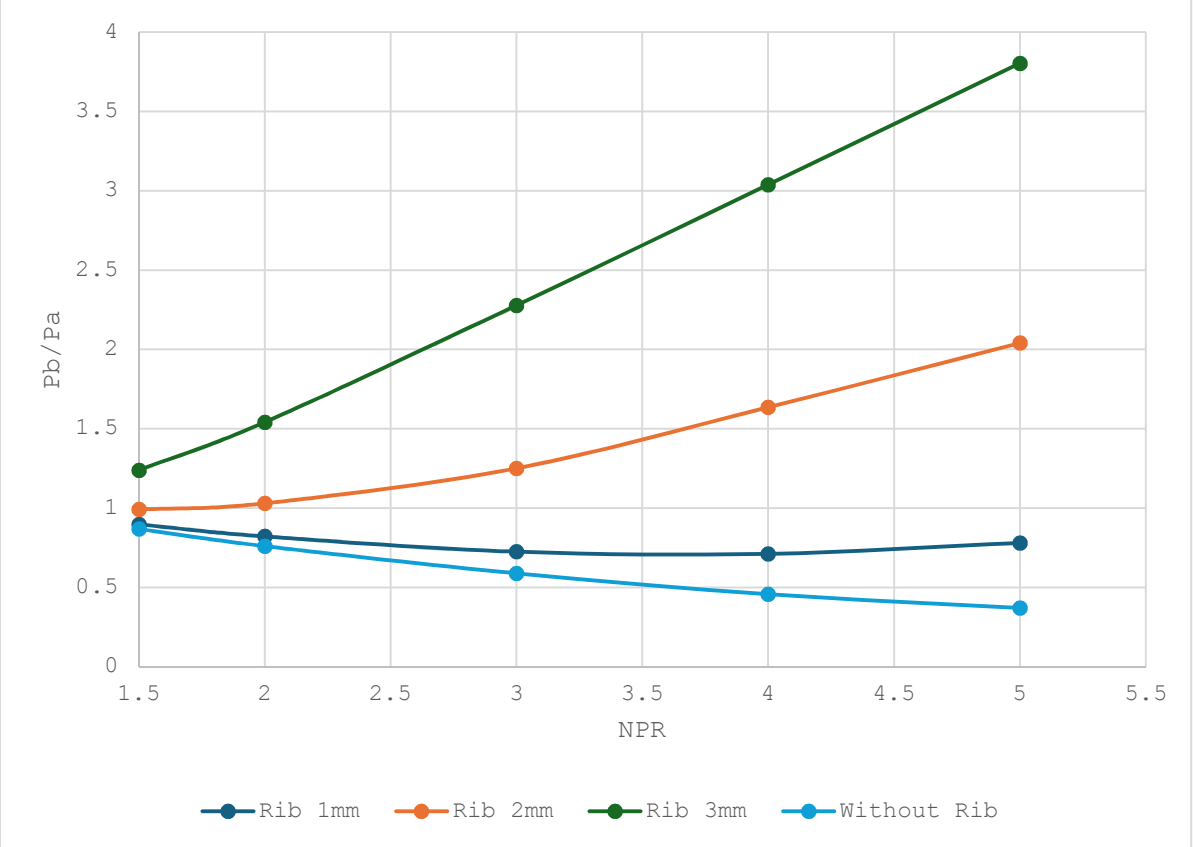
Pb/Pa
NPR
Rib 1mm
Rib 2mm
Rib 3mm
Without Rib

(b) L/D = 4

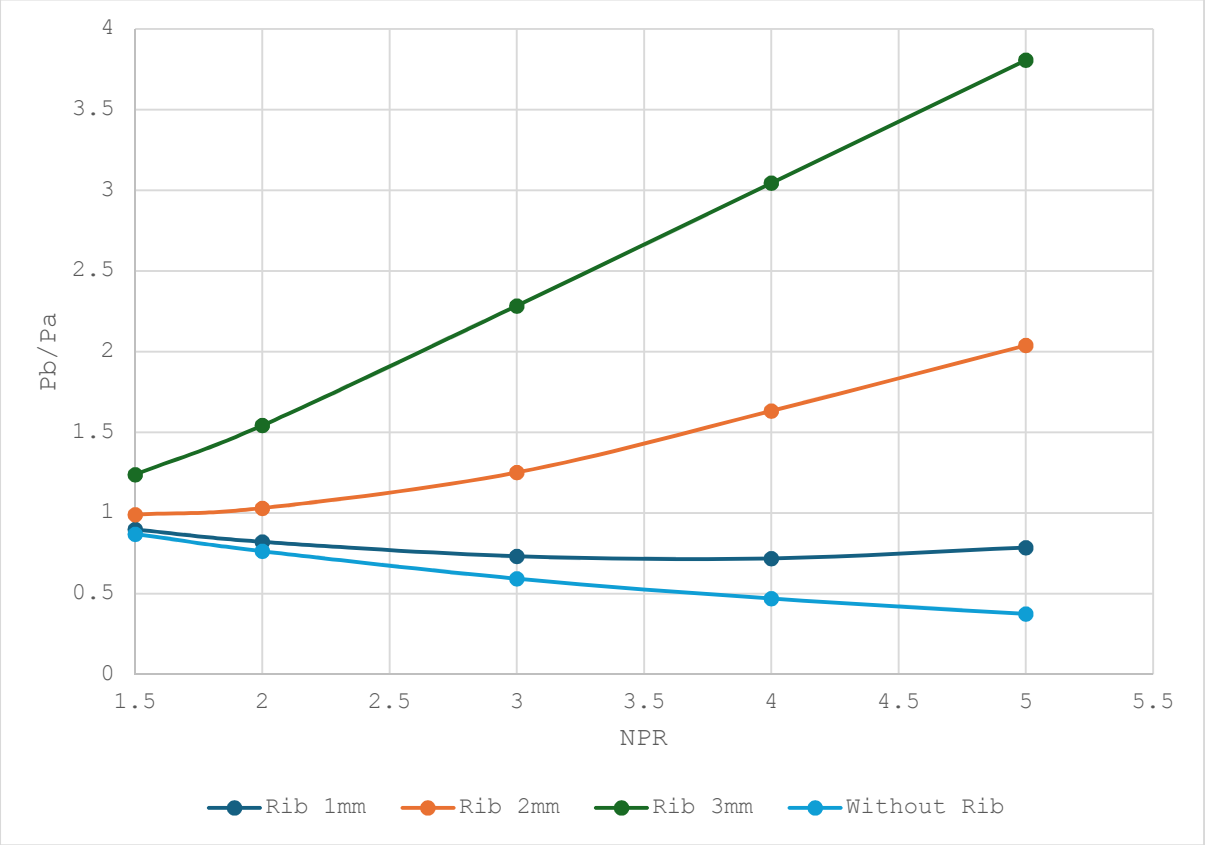
Pb/Pa
NPR
Rib 1mm
Rib 2mm
Rib 3mm
Without Rib

(c) L/D = 5

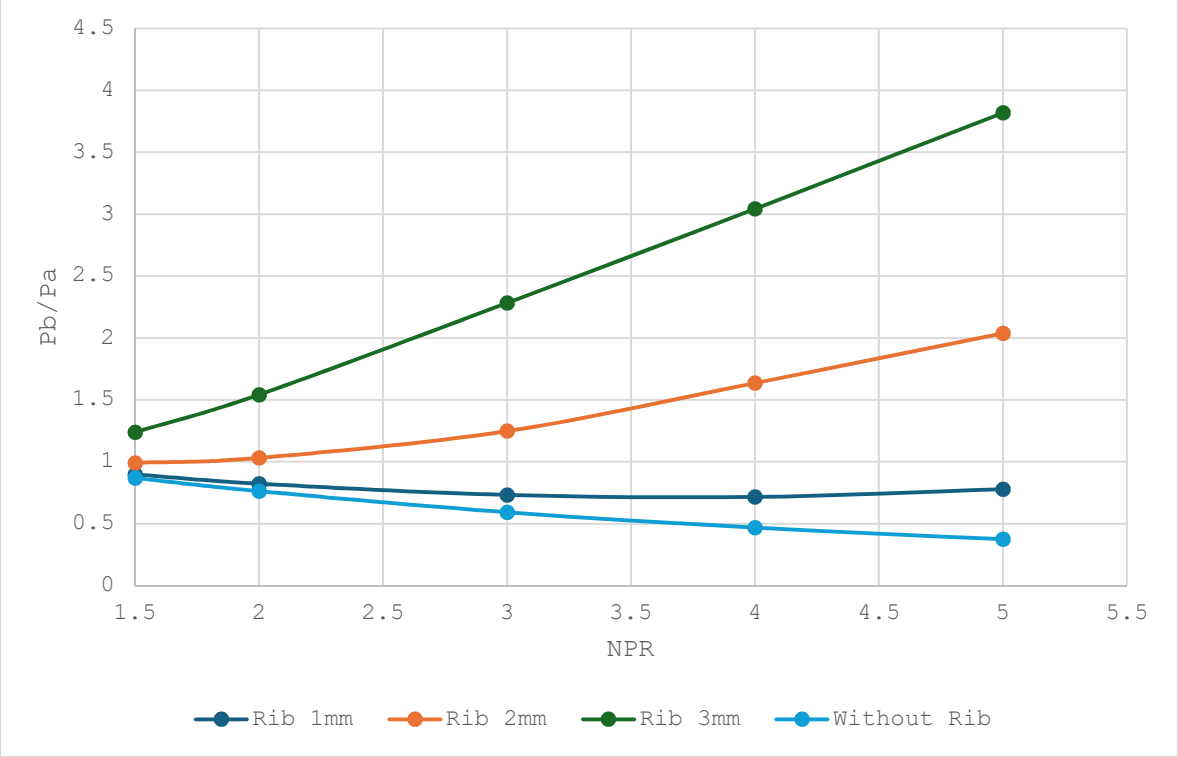

(d) L/D = 6

Fig. 11 Base Pressure Vs. NPR for numerous Duct segments

5.6 Base Pressure Results for Rib Location at L/D = 3.0

Finally, the outcomes of this study are presented in Figures 12(a) to (c) for the same range of nozzle pressure ratios and duct sizes, specifically L/D = 4, 5, and 6. As mentioned earlier, once the flow is established and the passive control, in the form of a D-shaped rib, is placed at L/D = 3, it does not yield encouraging results; there is no reverse flow from the reattachment point, which is necessary for this case to enhance the base pressure. Even though there is a marginal increase in the base pressure, it is not worth mentioning, as the gain achieved for the rib location at L/D = 1 and 1.5 remains almost the same, despite the rib being relocated towards the downstream end of the duct. The same is true for this location of the rib; with increasing duct sizes, there is not much change in the magnitude of the base pressure.

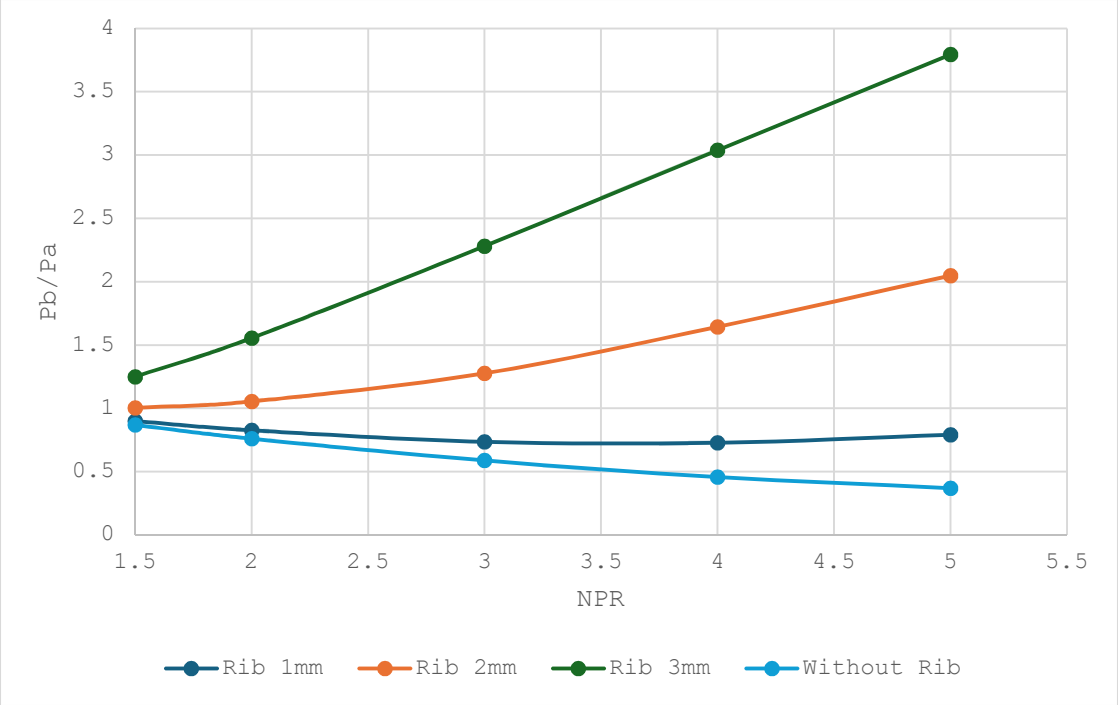
Pb/Pa
NPR
Rib 1mm
Rib 2mm
Rib 3mm
Without Rib

(a) L/D = 4

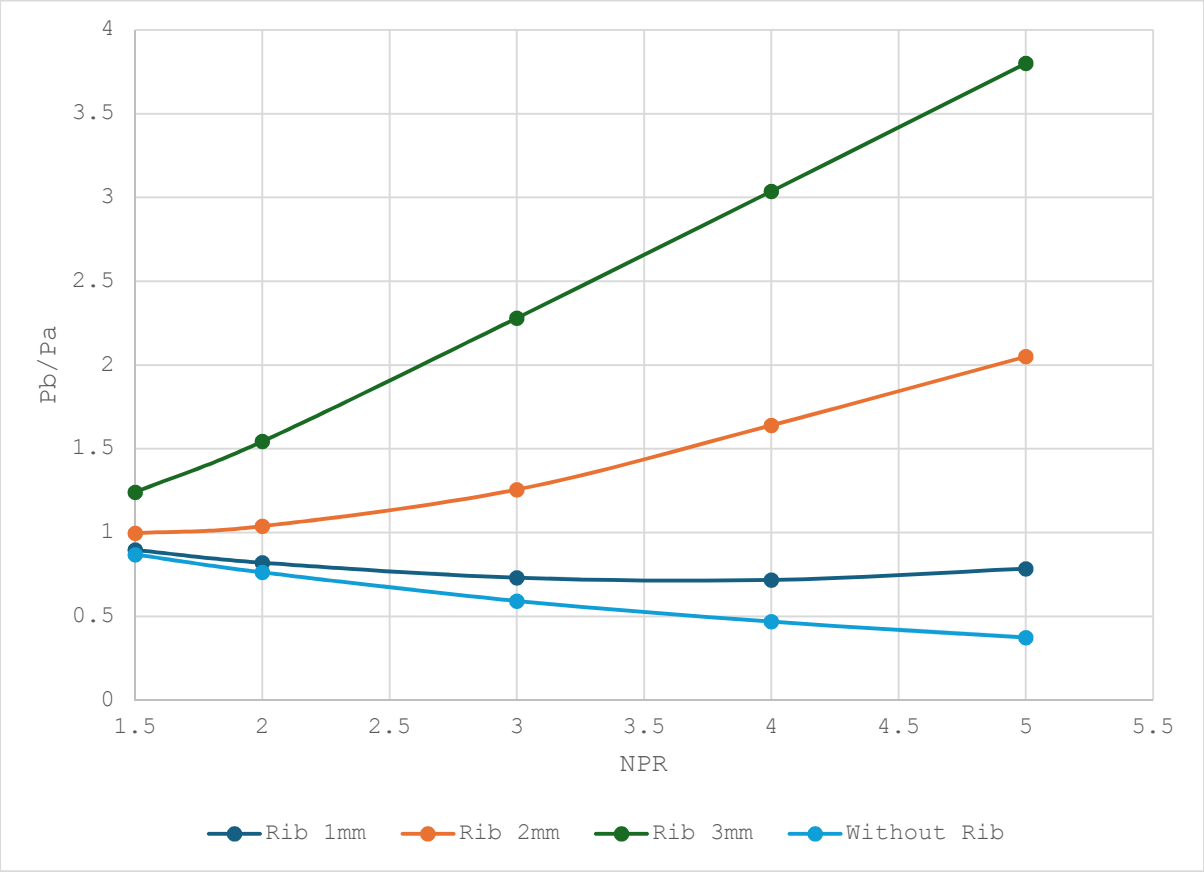
Pb/Pa
NPR
Rib 1mm
Rib 2mm
Rib 3mm
Without Rib

(b) L/D = 5

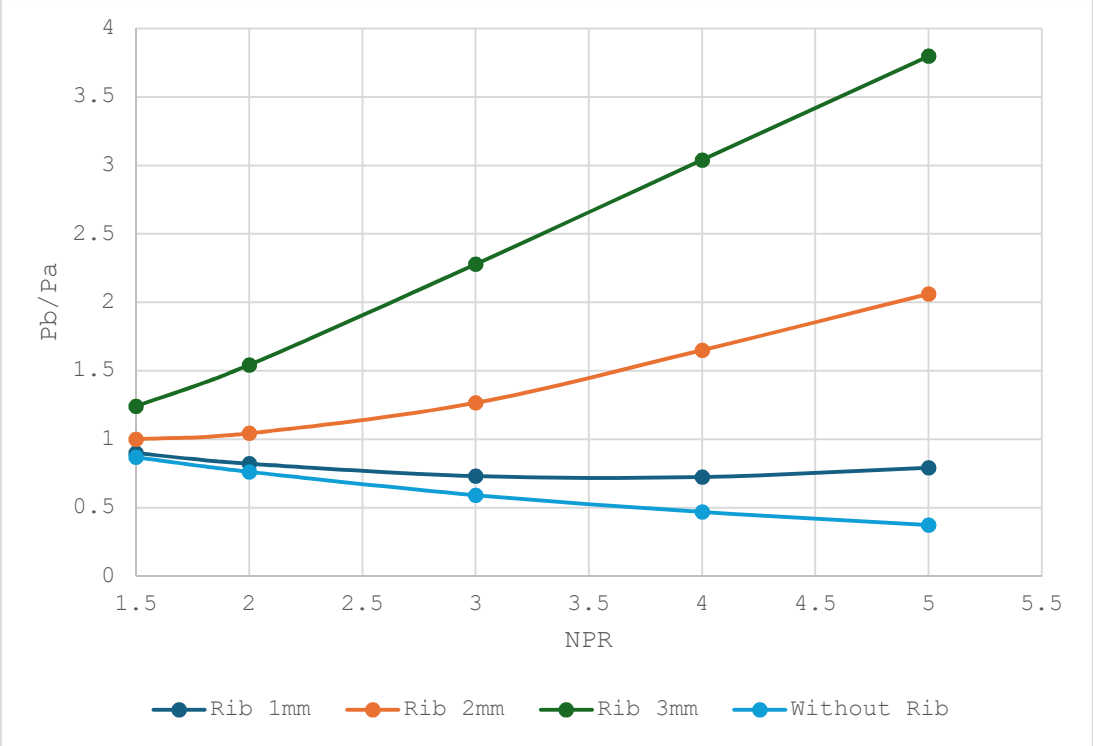

(c) L/D = 6

Fig. 12 Base Pressure Vs. NPR for numerous Duct segments

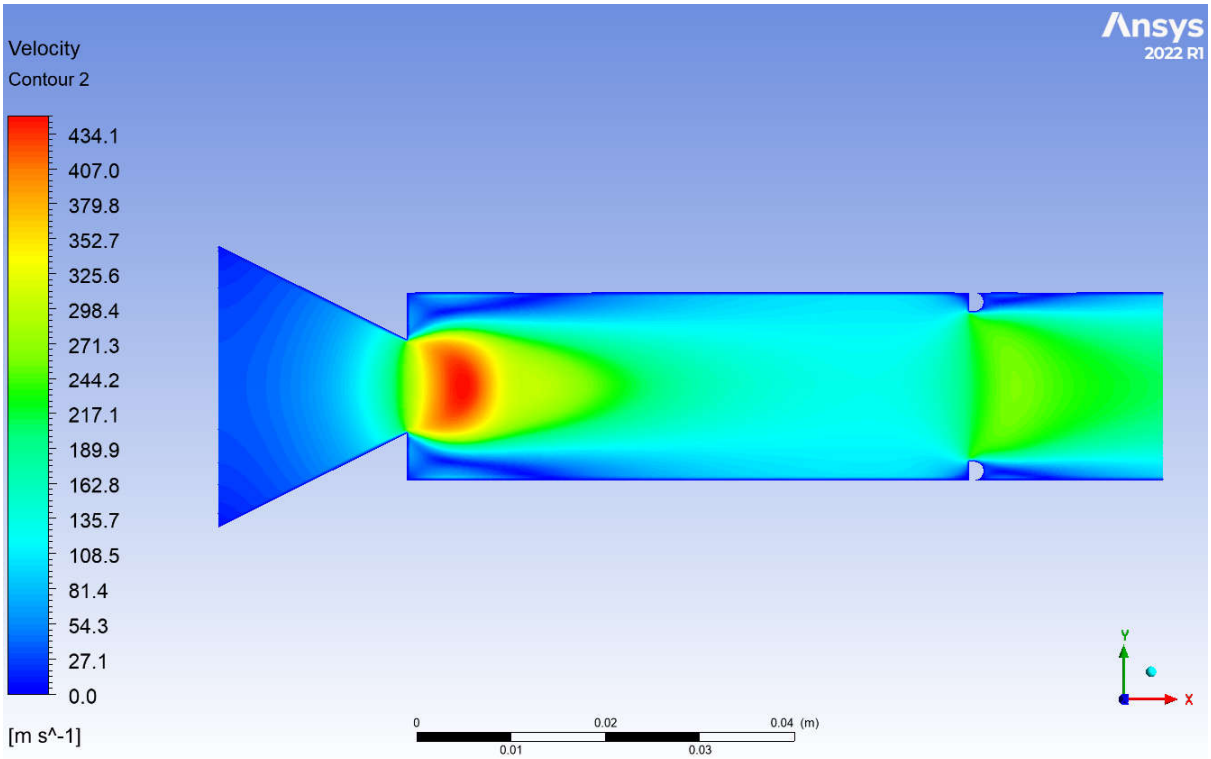

(a) Pressure Contour

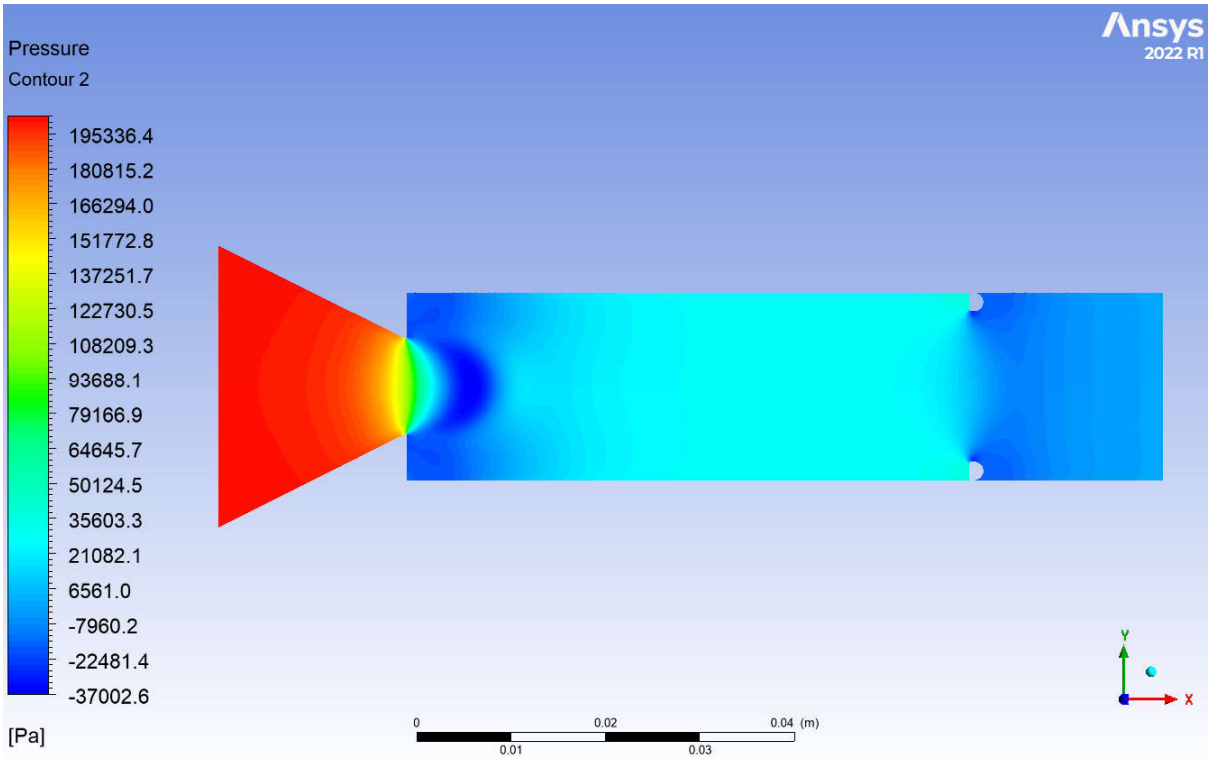

(b) Velocity Contour

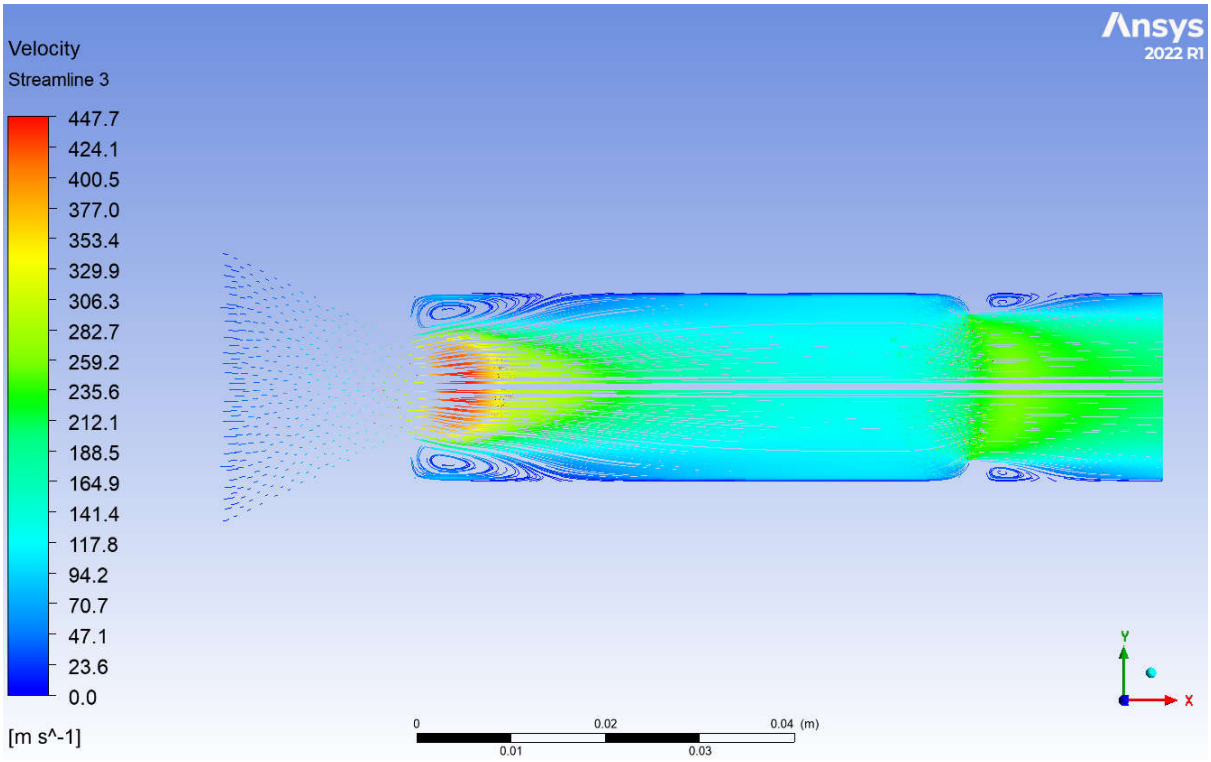

(c) Streamline Contour

Fig. 13 Pressure, Velocity, and Streamline Contour for Rib location at L/D = 3 and NPR = 3

Fig. 13 shows the pressure, velocity, and streamline contours for rib placement at L/D = 3 for rib radius of 1 mm. These figures clearly demonstrate the formation of low-pressure recirculation zones and a decrease in pressure at the base corner of the duct. It also shows the deceleration in the flow once exhausted into the enlarged duct. However, the main jet still contains sufficient kinetic energy despite the excessive losses due to the sudden expansion of the flow.

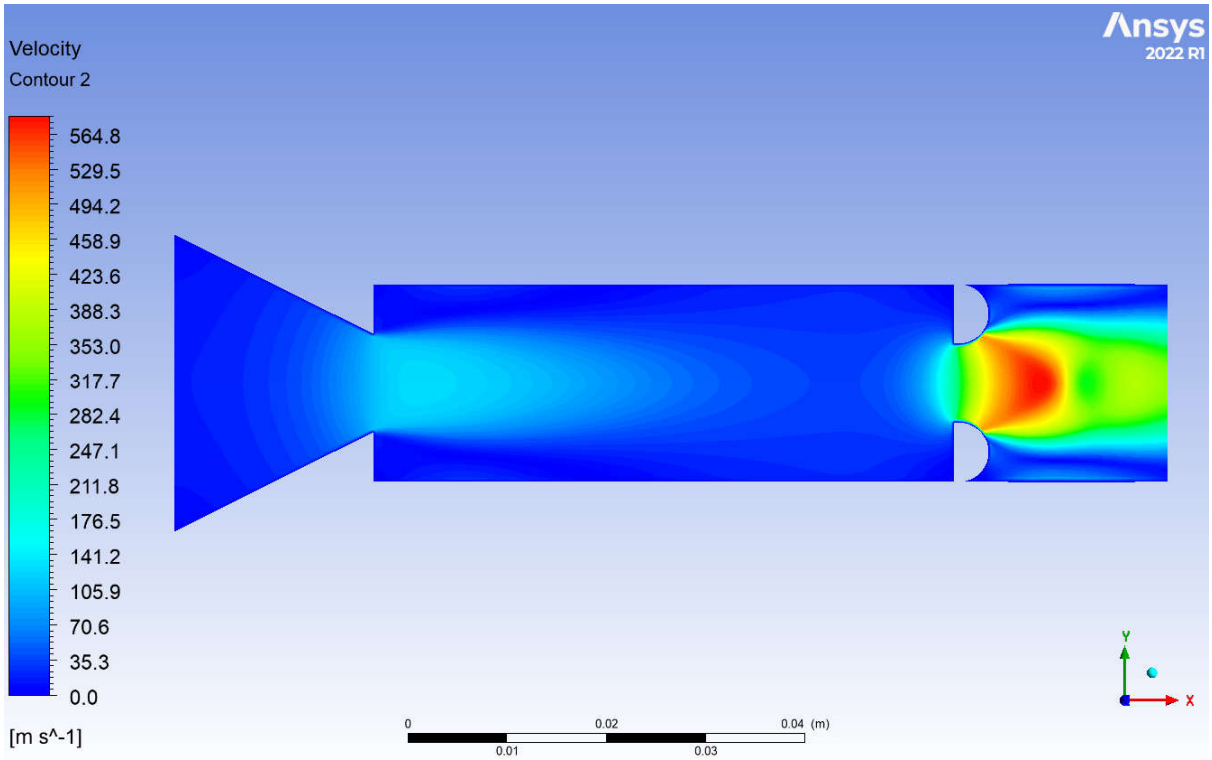

(a) Velocity contour

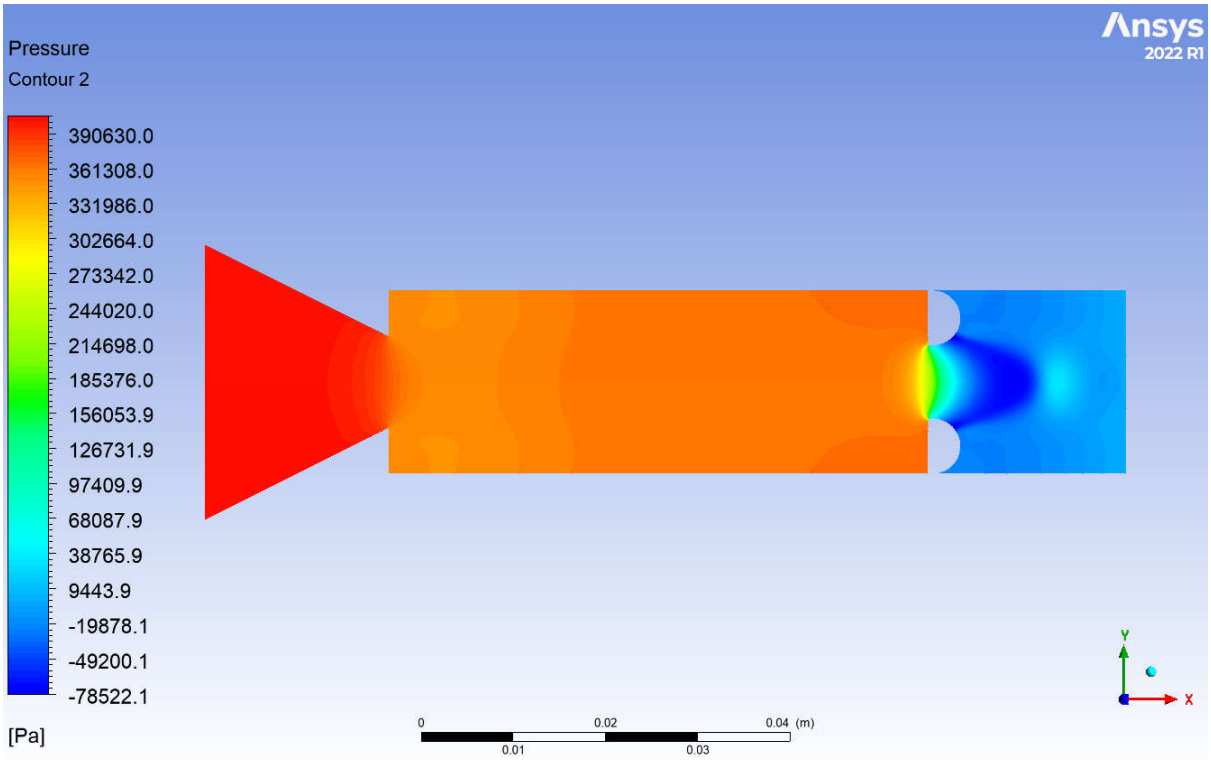

(b) Pressure contour

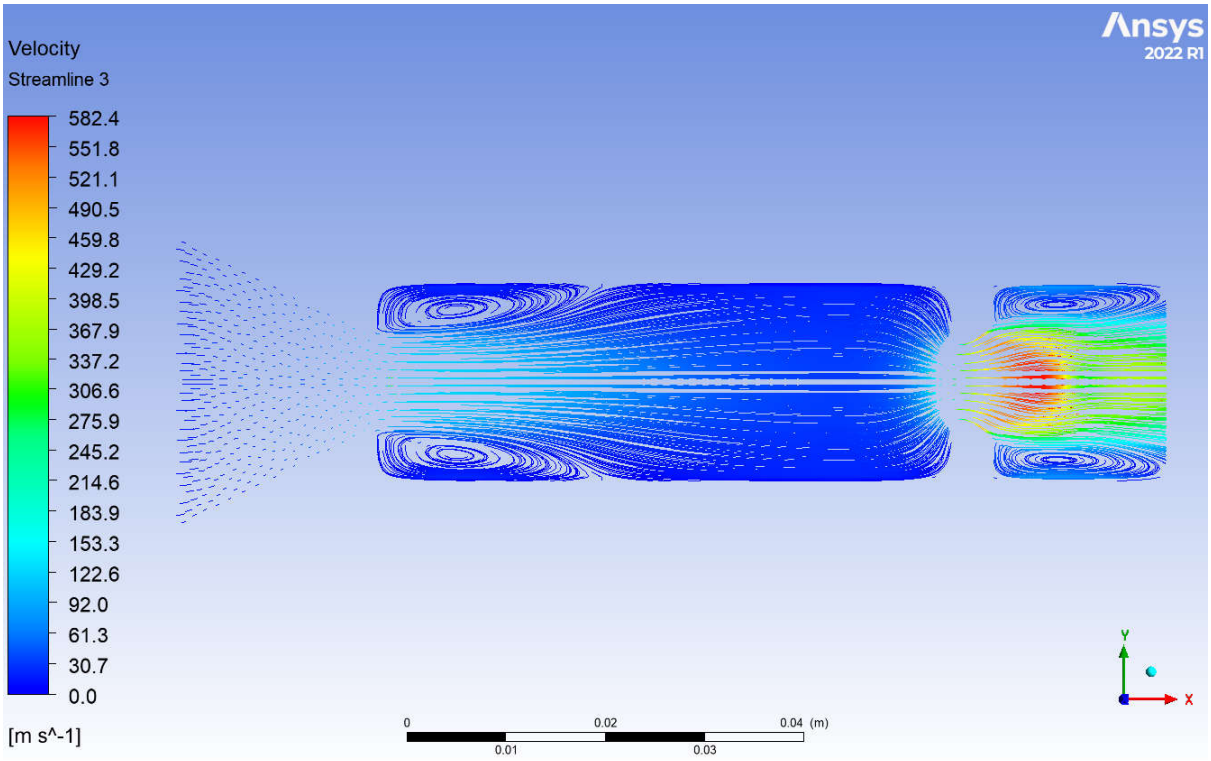

(c) Streamline Contour

Fig. 14 Pressure, Velocity, and Streamline Contour for Rib radius 3mm, rib location at L/D = 3 and NPR = 5

Fig. 14 displays the pressure, velocity, and streamline contours when the D-shaped rib of radius 3 mm is located at L/D = 3 for NPR = 5. For this NPR, the nozzle exiting the shear layer is underexpanded, and the flow must undergo expansion until its pressure equals the ambient pressure. The figure also shows the formation of the recirculation zone at the base of the duct and at the base of the rib. These recirculation zones reiterate that whenever the control blocks the flow, it will result in the formation of separated recirculation zones.

6. Conclusions: Based on the above deliberations, we may conclude that the base pressure is a strong function of the nozzle pressure ratio and the rib locations. In this study, we have considered two orientations of the rib. For orientation one, the curved part of the D-shaped rib faces the exiting shear layer from the converging nozzle, and the straight part of the rib faces the shear layer. The results show that the base pressure values are slightly higher for orientation two than for rib orientation. This change is due to the sharp corner being upstream and downstream for other orientations.

For this duct diameter, the reattachment length seems to be around L/D = 1 to 1.5. That may be the main reason that when the rib is shifted to L/D = 2 and 3, it does not substantially increase the base pressure. As we know, this increase in the base pressure is due to the interaction of the waves, the location of the reattachment point, the duct size, and the strength of the secondary vortices.

For rib location L/D = 0.5, the flow is in transition and has not been established; hence, the base pressure values are lower than the base pressure values for rib locations at L/D = 1 and 1.5.

There is a progressive rise in the base pressure values when the rib is located at L/D = 1, and then, when the rib is located at L/D = 1.5, there is a marginal change in the base pressure values. With a further shift in the rib locations downstream (i.e., L/D = 2 and 3), there is no change in the base pressure values, as they have reached a steady state. Hence, one suggestion is to analyze the results on a case-by-case basis. The reattachment length depends on the Mach number, duct diameter, expansion levels, and length-to-diameter ratio.

7. References

[1] Rathakrishnan, E. 2001. "Effect of Ribs on Suddenly Expanded Flows." AIAA Journal 39 (7): 1402–1404.
[2] Rathakrishnan, E. 1999. "Effect of Splitter Plate on Bluff Body Drag." AIAA Journal 37 (9): 1125–1126. https://doi.org/10.2514/2.823.
[3] Baig, M. A. A., S. A. Khan, Al-Mufadi, Fahad, and E. Rathakrishnan. 2011. "Control of Base Flows with Microjets." International Journal of Turbo Jet Engines 28 (1): 59–69. https://doi.org/10.1515/TJJ.2011.009.
[4] Rathakrishnan, E. 2015. "Base Pressure Control by Using Ribs in Subsonic and Sonic Suddenly Expanded Flows." AIAA Conference Proceedings.

[5] Vijayaraja, K., C. Senthilkumar, S. Elangovan, and E. Rathakrishnan. 2014. "Base Pressure Control with Annular Ribs." International Journal of Turbo Jet Engines 31 (2): 111–118. https://doi.org/10.1515/tjj-2013-0037.
[6] Sethuraman, V., P. Rajendran, S. A. Khan, A. Aabid, and M. Baig. 2024. "Control of Nozzle Flow Using Rectangular Ribs at Sonic and Supersonic Mach Numbers." Fluid Dynamics and Materials Processing. https://doi.org/10.32604/fdmp.2024.049441.
[7] Sethuraman, V., P. Rajendran, and S. A. Khan. 2020. "Base and Wall Pressure Control Using Cavities and Ribs in Suddenly Expanded Flows – An Overview." Journal of Advanced Research in Fluid Mechanics and Thermal Science 66 (1): 120–134.
[8] Khan, A., S. A. Khan, V. Raja, A. Aabid, and M. Baig. 2024. "Effect of Ribs in a Suddenly Expanded Flow at Sonic Mach Number." Heliyon 10 (9): e30313. https://doi.org/10.1016/j.heliyon.2024.e30313.
[9] Khan, A., A. Aabid, M. N. Akhtar, S. A. Khan, and M. Baig. 2025. "Supersonic Flow Control with Quarter Rib in a Duct: An Extensive CFD Study." International Journal of Thermofluids 26: 101060. https://doi.org/10.1016/j.ijft.2025.101060.
[10] Azami, M. H., M. Faheem, A. Aabid, I. Mokashi, and S. A. Khan. 2019. "Inspection of Supersonic Flows in a CD Nozzle Using an Experimental Method." International Journal of Recent Technology and Engineering 8 (2S3): 996–999.
[11] Pathan, K. A., P. S. Dabeer, and S. A. Khan. 2020. "Enlarge Duct Length Optimization for Suddenly Expanded Flows." Advances in Aircraft and Spacecraft Science 7 (3): 203–214.
[12] Khan, A., A. Aabid, S. A. Khan, M. N. Akhtar, and M. Baig. 2024. "Comprehensive CFD Analysis of Base Pressure Control Using Quarter Ribs in Sudden Expansion Duct at Sonic Mach Numbers." International Journal of Thermofluids 24 (October): 100908. https://doi.org/10.1016/j.ijft.2024.100908.
[13] Khan, A., S. A. Khan, M. N. Akhtar, A. Aabid, and M. Baig. 2024. "Base Pressure Control with Semi-Circular Ribs at Critical Mach Number." Fluid Dynamics and Materials Processing 22. https://doi.org/10.32604/fdmp.2024.049368.
[14] Khan, A., N. M. Mazlan, and E. Sulaeman. 2022. "Effect of Ribs as Passive Control on Base Pressure at Sonic Mach Numbers." CFD Letters 14 (1): 140–151. https://doi.org/10.37934/cfdl.14.1.140151.

[15] Hai-bo, and W.-q. Liu. 2012. "Influence of Cavity Length on Forward-Facing Cavity and Opposing Jet Combined Thermal Protection System Cooling Efficiency." International Journal of Aerospace and Mechanical Engineering.
[16] Heubner, L. D., and L. J. Utreja. 1993. "Mach 10 Bow Shock Behaviour of Forward-Facing Nose Cavity." Journal of Spacecraft and Rockets 30: 291–297. https://doi.org/10.2514/3.25513.
[17] Lorite, M., et al. 2017. "Drag Reduction of Slender Blunt-Based Bodies Using Optimized Rear Cavities." Journal of Fluids and Structures. https://doi.org/10.1016/j.jfluidstructs.2017.07.011.
[18] Sanmiguel, E., and M.-A. Alcantara. 2014. "Drag Reduction Induced by the Addition of a Multi-Cavity at the Base of a Bluff Body." Journal of Fluids and Structures. https://doi.org/10.1016/j.jfluidstructs.2014.03.013.
[19] Kavimandan, M., and B. Chandrasheker. 2020. "Aerothermodynamic Analysis of a Blunt Body with Forward-Facing Cavity and Opposing Jet Combination." International Journal of Engineering Research and Technology (IJERT).
[20] Saravanan, G., G. Jagadeesh, and K. P. J. Reddy. 2009. "Investigation of the Missile-Shaped Body with Forward-Facing Cavity at Mach 8." Journal of Spacecraft and Rockets 46: 577–591. https://doi.org/10.2514/1.38914.

[21] Sudarshan, S., and S. M. V. Rao. 2021. "Effect of the Axial Cavity with an Opposing High-Pressure Jet Combination in a Mach 6 Flow Condition." Acta Astronautica. https://doi.org/10.1016/j.actaastro.2020.09.021.
[22] Mohandas, S., and B. John. 2019. "Reduction of Wave Drag on Parameterized Blunt Bodies Using Spikes with Varied Tip Geometries." Acta Astronautica. https://doi.org/10.1016/j.actaastro.2019.04.017.
[23] Engblom, W. A., B. Yuceil, D. B. Goldstein, and D. S. Dolling. 1995. "Hypersonic Forward-Facing Cavity Flow: An Experimental and Numerical Study." AIAA Paper 95-0293. https://doi.org/10.2514/6.1995-293.
[24] Huang, W., and Z.-t. Zhao. 2017. "Parametric Study on the Drag and Heat Flux Reduction Mechanism of a Forward-Facing Cavity on a Blunt Body in Supersonic Flows." Aerosp. Science and Technology. https://doi.org/10.1016/j.ast.2017.10.017.
[25] Santos, W. F. N. 2007. "Simulation of Blunt Leading Edge Aerothermodynamics in Rarefied Hypersonic Flow." Journal of the Brazilian Society of Mechanical Sciences and Engineering 29 (2): 39–51. https://doi.org/10.1590/S1678-58782007000200001.
[26] Khan, S. A., Asadullah, M., Fharukh Ahmed, G.M., Jalaluddeen, Ahmed, Ali Baig, Maughal Ahmed. 2018. "Passive Control of Base Drag in Compressible Subsonic Flow Using Multiple Cavities." International Journal of Mechanical and Production Engineering Research and Development 8 (4): 39–4431.
[27] Khan, S. A., Asadullah, M., Sadiq, J. 2018. "Passive Control of Base Drag Employing Dimple in Subsonic Suddenly Expanded Flow." International Journal of Mechanical and Mechatronics Engineering 18 (3): 69–74.
[28] Sajali, M. F. M., Aabid, A., Khan, S. A., Mehaboobali, F. A. G., Sulaeman, E. 2019. "Numerical Investigation of the Flow Field of a Non-Circular Cylinder." CFD Letters 11 (5): 37–49.
[29] Khan, S. A., and E. Rathakrishnan. 2006. "Nozzle Expansion Level Effect on Suddenly Expanded Flow." International Journal of Turbo Jet Engines 23 (4): 233–257
[30] Khan, S. A., and E. Rathakrishnan. 2005. "Active Control of Suddenly Expanded Flow from Under-Expanded Nozzles—Part II." International Journal of Turbo Jet Engines 22 (3): 163–183. https://doi.org/10.1515/TJJ.2005.22.3.163.